DIEGO BARBOSA CARVALHO

PROPOSED MODEL WITH WEIGHTED PARAMETERS FOR MICROGRID MANAGEMENT: INCORPORATING DIVERSE LOAD PROFILES, ASSORTED TARIFF POLICIES, AND ENERGY STORAGE DEVICES

Itajubá, MG, Brazil

2024

FEDERAL UNIVERSITY OF ITAJUBÁ

ELECTRIC AND ENERGY SYSTEM INSTITUTE

DIEGO BARBOSA CARVALHO

Proposed model with weighted parameters for microgrid management: incorporating diverse load profiles, assorted tariff policies, and energy storage devices

Thesis submitted to the Graduate Program in Electrical Engineering as part of the requirements for obtaining the degree of Doctor of Science in Electrical Engineering.

Supervisor/Adviser Professor: EDSON DA COSTA BORTONI

Itajubá, MG, Brazil

2024

DEDICATIONS

I dedicate this doctoral thesis to God and my parents.

ACKNOWLEDGMENT

RESUMO

Este estudo apresenta um modelo baseado em otimização com parâmetros ponderados e ajustáveis, incorporando variantes determinísticas e estocásticas para permitir uma transição suave entre estratégias de controle para o gerenciamento de microrredes. A motivação para conduzir este estudo surge de uma lacuna identificada na literatura sobre o gerenciamento de microrredes, especialmente porque poucos estudos abordam cargas não programadas sob diferentes políticas de mercado de energia. Considerando esse fator, o objetivo da pesquisa é verificar as vantagens técnicas e econômicas que a abordagem proposta oferece a uma microrrede caracterizada por um perfil de carga que sofre variações significativas com base no dia da semana. Um sistema de controle baseado em Model Predictive Control (MPC) é empregado como o gerente do sistema, utilizando indicadores-chave de desempenho para avaliar a eficácia do modelo. A estratégia de controle, implementada no nível do gerador de sinal de referência, é projetada para minimizar os custos operacionais e conter a degradação do Sistema de Armazenamento de Energia (ESS). Os resultados demonstram que a variante determinística do modelo proposto proporciona um retorno quantitativo significativo para a microrrede, especialmente em perfis de carga mais estáveis. Além disso, a variante determinística é um método que permite elucidar uma variedade de valores para os parâmetros ponderados do modelo proposto, que serão utilizados na variante estocástica da abordagem. Por outro lado, a variante estocástica destaca-se por oferecer benefícios mais pronunciados para a microrrede em cenários com perfis de carga com variações abruptas. Ambas as versões do modelo em estudo exibem desempenho notável em comparação com os modelos de referência estabelecidos.

Palavras-chave: Microrrede, Estratégia de Gerenciamento de Energia, Modelo de Controle Preditivo, Sistema de Armazenamento de Energia

ABSTRACT

This study introduces an optimization-based model featuring weighted and adjustable parameters, integrating deterministic and stochastic components to facilitate a seamless transition between control strategies for microgrid management. The impetus for this investigation stems from a discerned void in the existing literature concerning microgrid management, particularly the scarcity of studies addressing non-scheduled loads within various energy market frameworks. In light of this gap, the research aims to evaluate the technical and economic merits of the proposed approach within a microgrid characterized by a load profile exhibiting significant day-of-the-week variations. A Model Predictive Control (MPC)-based control system serves as the central management entity, utilizing key performance indicators to gauge the efficacy of the model. This control strategy, implemented at the reference signal generator level, is devised to minimize operational expenses and mitigate degradation of the Energy Storage System (ESS). The findings indicate that the deterministic variant of the proposed model yields considerable quantitative benefits for the microgrid, particularly evident in scenarios with more stable load profiles. Moreover, the deterministic variant facilitates the elucidation of a range of values for the weighted parameters of the model, subsequently utilized in the stochastic variant. Conversely, the stochastic variant emerges as particularly advantageous for the microgrid in situations characterized by abrupt load profile changes. Both iterations of the model under investigation demonstrate noteworthy performance compared to established benchmark models.

Keywords: Microgrid, Energy Management Strategy, Model Predictive Control, Energy Storage System

LIST OF FIGURES

LIST OF TABLES

LIST OF ABBREVIATIONS

PV	Photovoltaic
STC	Standard Test Condition
NOCT	Nominal Operating Cell Temperature
ESS	Energy Storage System
EGS	Energy Generating System
MPC	Model Predictive Control
MG	Microgrid
RMSE	Root Mean Squared Error
SOC	State of Charge
KPI	Key Performance Indicator

<h1>LIST OF SYMBOLS</h1>

A_r	Area swept by the turbine blades (m²)
C_p	Power coefficient
d	Diameter of the area swept by the Wind turbine blades (m)
G	Incident irradiance (W/m^2)
G_{NOCT}	Irradiance in which the cell temperature is the NOCT (W/m^2)
G_{STC}	Incident irradiance in STC (1000 W/m^2)
NOCT	Normal Operating Cell Temperature (ºC)
N_{pv}	Number of PV panels connected in the PV array
P_{wind}	Electric power generated by the turbine (W)
P_w	Electric power generated by the turbine considering the features of the machine (W)
P_{pv}	PV power provided by a solar panel (W)
P_{STC}	Cell maximum power in STC (W)
P_{wind_rated}	Turbine rated power (W)
T_{amb}	Ambient temperature (ºC)
$T_{amb,NOCT}$	Ambient NOCT equal to 25ºC
T_{cell}	Cell temperature (ºC)
v	Wind speed that crosses the turbine area (m/s)
$v_{cut\text{-}in}$	The turbine cut-in speed (m/s)
$v_{cut\text{-}out}$	The turbine cut-out speed (m/s)
v_r	The turbine rated speed (m/s)
γ	Coefficient of maximum power (1/ºC)
ρ	Air density (kg/m³)
E	Voltage source (V)
$R_{p(bat)}$	Battery parallel equivalent resistance (Ω)
C_{bat}	Battery parasitic capacitance (F)
$R_{s(bat)}$	Battery series equivalent resistance (Ω)
V_{Cbat}	Battery capacitor voltage (V)
i_{Cbat}	Current flowing through the battery capacitor (A)
V_{bat}	Battery voltage that is supplied to the load (V)
i_{bat}	Battery current supplied to the load (A)

C_{UC}	Ultra-capacitor capacitance (F)
$R_{p(UC)}$	Ultra-capacitor parallel equivalent resistance (Ω)
$R_{s(UC)}$	Ultra-capacitor series equivalent resistance (Ω)
i_{UC}	Current that traverses the ultra-capacitor (A)
i_{RpUC}	Current that flows through the parallel resistor (A)
i_{load}	Current provided to the load (A)
V_{UC}	Voltage across the ultra-capacitor (V)
V_{load}	Voltage provided to the load (V)
P_{bat}	Power delivered by the battery (W)
P_{UC}	Power delivered by the ultra-capacitor (W)
$\tau_{1(bat)}$	Variable that represent i_{bat} in the battery linearization equation (A)
$\tau_{1(UC)}$	Variable that represent i_{bat} in the UC linearization equation (A)
$\tau_{2(bat)}$	Variable that represent i_{C} in the battery linearization equation (A)
$\tau_{2(UC)}$	Variable that represent i_{C} in the UC linearization equation (A)
P_{grid}	Grid power (W)
P_{total}	Total power, which is the balance of power between the power generated by the EGS and the power consumed by the load (W)
y_{ref}	Control reference signal (W)
W_{y}	Positive weight matrices of the output
W_{u}	Positive weight matrices of the input
q_{rbat}	Charge capacity of the battery (Ah)
q_{rUC}	Charge capacity of the ultra-capacitor (Ah)
$soc_{min(bat)}$	Minimum charge level that can be attained by the battery
$soc_{max(bat)}$	Maximum charge level that can be attained by the battery
$soc_{min(UC)}$	Minimum charge level that can be attained by the ultra-capacitor
$soc_{max(UC)}$	Maximum charge level that can be attained by the ultra-capacitor
m_{p}	MPC prediction horizon
m_{c}	MPC control horizon
$y(k)$	MPC output (W)
$y(k+n)$	Future prediction of MPC output (W)
$p_{tariff}(t)$	Energy tariff price at time t (US\$/kWh)
δ	Grid power's weighting parameter
α	Battery SOC's weighting parameter

β	UC SOC's weighting parameter
Pr_{bat}	Battery average power (W)
Pr_{UC}	UC average power (W)
$P_{grid,res.}$	Reset P_{grid} (W)
$P_{total,res.}$	Reset P_{total} (W)
KPI^{sc1}	Economic metric to evaluate the economic feasibility of the microgrid in scenario 1 (US$)
KPI^{sc2}	Economic metric to evaluate the economic feasibility of the microgrid in scenario 2 (US$)
KPI^{sc1}_{cycle}	Key performance indicator for scenario 1, normalized by the number of ESS cycles (US$)
KPI^{sc2}_{cycle}	Key performance indicator for scenario 2, normalized by the number of ESS cycles (US$)
$KPI_{stch/cycle}$	Key Performance Indicator derived from the stochastic algorithm, normalized based on the total number of ESS cycles (US$)
KPI_{stch}	Key Performance Indicator used during the implementation of the stochastic model (US$)
$Cost_{Pgrid}^{sc1}$	Cost of the grid power over a day in scenario 1 (US$)
$Cost_{Pgrid}^{sc2}$	Cost of the grid power over a day in scenario 2 (US$)
$Cost_{Ptotal}^{sc1}$	Cost of the total power over a day in scenario 1 (US$)
$Cost_{Ptotal}^{sc2}$	Cost of the total power over a day in scenario 2 (US$)
$Cost_{Pgrid}^{MC}$	Cost of the grid power over the last hour as MC runs (US$)
$Cost_{Ptotal}^{MC}$	Cost of the total power over the last hour as MC runs (US$)
p_{off_peak}	Tariff price over the off-peak period of the day (US$/kWh)
p_{peak}	Tariff price over the peak period of the day (US$/kWh)
p_{tariff}^{mc}	Tariff price as MC runs (US$/kWh)

TABLE OF CONTENTS

1 Introduction

1.1 Contextualization of the theme and related works

Microgrids are highly complex and intricate systems of power distribution, designed to seamlessly integrate a diverse range of loads and distributed energy resources. These systems are regulated through a variety of control units, regardless of their connection to primary or isolated power grids. The integration of such systems necessitates the utilization of advanced control techniques to ensure efficient and reliable operation, and to optimize energy management in both grid-connected and islanded modes of operation.

In light of the growing apprehension surrounding environmental concerns and amplified competition in energy generation, the incorporation of renewable sources, such as wind and solar, into power systems has been increasingly favored. Furthermore, energy storage has emerged as a valuable tool in mitigating the disruptive impacts of grid oscillations, curbing energy wastage, and enhancing the technical and economic aspects of the power system. In this context, microgrids have garnered increasing recognition on a global scale and have been the subject of numerous academic inquiries, particularly concerning their management strategies.

Some advantages of microgrids include (GUERRERO et al., 2013; LASSETER, 2011; PARHIZI et al., 2015):

- Improved reliability and resiliency: microgrids (MGs) can operate autonomously in case of a power outage in the primary grid, providing a reliable source of power to critical loads;

- Enhanced energy efficiency: MGs can use distributed energy resources (DERs) like solar and wind power, which can be more efficient and reduce transmission losses.

- Cost savings: By generating power locally, microgrids can reduce the need for expensive transmission and distribution infrastructure, resulting in cost savings.

- Increased use of renewable energy: MGs can incorporate renewable energy sources, reducing reliance on fossil fuels and reducing greenhouse gas emissions.

- Grid support and stability: MGs can provide grid support by stabilizing voltage and frequency, reducing the risk of blackouts and brownouts.

- Energy security: MGs can provide energy security for critical facilities like hospitals, military bases, and data centers, ensuring uninterrupted power supply in case of a disruption in the primary grid.

Regarding the operation of MGs, K/bidi et al. (2022) have employed an energy management strategy to operate a MG, which consists of a photovoltaic (PV) array, full cells, and an Electrolyzer as an Energy Storage System (ESS). The primary objective of the proposed strategy is to address a unit commitment problem while also considering the constraints of the microgrid devices. By utilizing key performance indicators, the findings of the study indicate that the implemented energy management system can effectively prevent unsatisfactory start-up of the full cells and the Electrolyzer. Chen; Dong; Yang (2022) have presented a study that employs a model to define the characteristics of renewable power generation and uncertainties. The study's findings reveal that the proposed solution can optimize the maximum utilization efficiency of renewable energy while minimizing both economic cost and carbon emissions. Ali Dashtaki et al. (2023) have conducted a study that examines a novel microgrid management strategy utilizing an optimization approach with the goal of minimizing the overall operational and planning costs of the microgrid system. The research findings indicate that the proposed methodology can effectively decrease the total operational cost of the distribution network and reduce the overall power losses. Zhao; Wang; Guo (2023) present a study that focuses on microgrid energy management. The research proposes a hierarchical optimization configuration of a multi-energy microgrid system that takes into account the electricity market. The study findings reveal that the implemented approach can generate savings of around 3.5% in the microgrid system. Zhong et al. (2022) suggest an optimal energy management strategy for minimizing the operation cost of a network, taking into account operational constraints and carbon emissions. The study results indicate that the proposed methodology is effective in reducing both the operational costs and carbon emissions.

Fang et al. (2022) present a multiple time-scale energy management approach for a hydrogen-based MG to provide electricity, hydrogen, and heating loads, while minimizing the operational costs of the microgrid. The proposed approach also takes into account uncertainties related to renewable energy generation and demand. Leonori et al. (2020) conducted a study on various strategies for implementing a rule-based energy management system through a hierarchical genetic algorithm to maximize profit generated by energy exchange with the grid. The study considered a time-of-use energy pricing policy and aimed to reduce the complexity of the rule-based system. The results indicated that the performance was only slightly

lower than the optimal reference solution, even when the rule-based system was reduced in complexity. Kumar and Bae (2022) implemented a MPC-based approach to manage the operation of a MG that contains hybrid energy storage systems. This approach is responsible for controlling power electronics, such as DC-DC converters and grid-connected inverters. The effectiveness of the proposed energy management system was validated under different operating scenarios, and it was found to be effective in controlling the microgrid. Torkan; Ilinca; Ghorbanzadeh (2022) proposed a multi-objective genetic algorithm to solve technical and economic problems of a MG. The study considered demand response programs, reactive loads, and uncertainties from renewable energies. The results showed that participation in demand response programs and the use of reactive loads can reduce the costs of generation, reservation, and startup, as well as the level of pollution. The proposed algorithm effectively addressed the trade-offs between different objectives and helped in achieving a well-balanced solution.

Cai; Kordabad; Gros (2023) presents an energy management strategy for residential microgrid systems using a combination of Model Predictive Control-based Reinforcement Learning and Shapley value. The strategy is designed to address various challenges in residential microgrid systems, such as fluctuating spot-market prices, uncertain user demand and renewable generation, and collective peak power penalties. The ultimate goal is to optimize benefits for all residential prosumers by formulating the energy management problem as a Cooperative Coalition Game. The strategy aims to find an energy trading policy that reduces the collective economic cost, including spot-market cost and peak-power cost, of the residential coalition. Finally, the profits obtained through cooperation are distributed to all residents. The results of the simulations indicate that the MPC-based Reinforcement Learning approach proposed in this study is highly effective in reducing long-term economic costs, achieving a reduction of approximately 17.5%. Additionally, the use of the Shapley value method provides a fair solution for allocating collective bills amongst residential prosumers. Jain; Saxena (2023) provides a comprehensive review of various control schemes used in MG systems. The review covers primary control schemes used for regulating current or voltage, secondary control schemes used for correcting voltage or current errors, power-sharing schemes, and tertiary control schemes used for managing power flow and energy in a hybrid MG system. The work investigates specific control factors, including mode transition and coordinated control between multiple interlinking converter and energy storage systems. The main concern of MG systems is system stability, and therefore, a thorough understanding of control strategies is

essential for system engineers. The paper highlights control strategies, rotor angle, voltage and frequency instability in power systems, and methods for improving stability in MG systems. Legry et al. (2023) introduces a novel approach for microgrid control through a Model Predictive Supervisor. The supervisor is designed to incorporate internal objectives and enforce a virtual droop control at the Point of Common Coupling. The supervisor includes a prediction module based on a model of the microgrid and an outer loop that regulates the power supply to the Point of Common Coupling based on the aggregated capability diagram at the Point of Common Coupling. This approach provides a more efficient control scheme for microgrids, ensuring stability and optimal operation.

Khokhar; Parmar (2023) investigates the effects of a diverse mix of two commonly used energy storage units on the dynamic responses of an islanded MG. To address this challenge, the paper proposes a novel approach that employs a discrete-time Laguerre functions-based intelligent model predictive control (LiMPC) approach as a secondary controller. The simulation results demonstrate that the LiMPC approach based on energy storage is highly effective in enhancing the dynamic responses of the MG. The results validate the efficacy of the proposed approach, which can help to improve the stability and efficiency of MGs. Huang et al. (2023) proposes an improved model predictive control based optimal scheduling framework which incorporates a scheduling correction algorithm into the basic MPC structure. This framework is utilized for implementing economic and resilient scheduling of a hydrogen-based microgrid under normal and emergency conditions, respectively. The results of the study show that the proposed scheduling scheme is highly effective in reducing daily operation costs by 68% under normal conditions. Additionally, the scheme proactively allocates distributed energy sources in the hydrogen-based microgrid, which significantly reduces load shedding during emergency conditions.

In order to facilitate the advancement of energy management and enhance the operation of MGs, it is essential to implement control methodologies into the power system. To this end, controllers that rely on model predictive control have garnered extensive recognition in academic research owing to their ability to regulate limitations and handle outputs while taking into account the interdependencies between system variables. Stochastic (HE et al., 2022; JIAO et al., 2022; POLIMENI et al., 2021; TOSTADO-VÉLIZ et al., 2022) and deterministic (OSAKA; OHTA, 2015) MPC techniques are implemented in a broad range of applications, including MG systems (ERAZO-CAICEDO; MOJICA-NAVA; REVELO-FUELAGÁN, 2022; HE et al., 2023; NAWAZ et al., 2023; ZHAO et al., 2022), electric vehicles (DANTE et

al., 2022; HU et al., 2020; RITTER et al., 2022), power plants (JOSÉ; F. CAMACHO, 2020; LÓPEZ-BAUTISTA; FLORES-TLACUAHUAC; GUTIÉRREZ-LIMÓN, 2020; SHETGAONKAR et al., 2023; VIEIRA; BORTONI; BRETAS, 2019), and many others.

MPC is a control technique that utilizes an objective function to determine the control inputs to minimize its value. The specific form of the objective function depends on the control strategy employed for the system being controlled. Typically, a reference signal is used to guide the controller's response. In this context, the reference signal is a critical element in the operation of MGs and has been the subject of numerous academic investigations.

Khatamianfar et al. (2013) have presented a rule-based approach for generating a reference signal to be utilized by a MPC-based controller responsible for managing the power dispatch of a wind farm. The proposed methodology aims to optimize the sale of energy during peak demand or high-price periods and store it during off-peak periods to improve the overall efficiency of the system. The research results demonstrated that the proposed approach provides greater long-term profitability for the wind farm. Mansoorhoseini; Mozafari; Mohammadi (2022) have implemented a supervisory control technique to establish set-points and regulate voltage and frequency to their nominal values while simultaneously reducing generation costs. The sensitivity analysis conducted during the study demonstrated that the approach utilized by the researchers permits both AC and DC voltages to be economically and technically feasible. Shan; Hu; Liu (2022) have presented a comprehensive power control and optimization strategy for microgrids. The study utilizes an evolutionary optimization algorithm at the system level to generate the optimal set-points for active and reactive power, which are subsequently sent to the device level for controlling inverters. The research findings demonstrate the feasibility and effectiveness of the proposed power control and optimization strategy. Cao et al. (2020) have introduced a method that employs MPC to determine the optimal size of a battery energy storage system. The study utilizes a two-layer control closed-loop, with the outer layer comprising a PI controller that generates a reference signal to the MPC. The research findings are presented using a sizing decision map, allowing the most economical size of the battery energy storage system to be determined. The primary objective of Nahata et al. (2021) is not to investigate the reference signal, but rather to establish a hierarchical control architecture that encompasses the entire system. One of the layers of the proposed architecture generates optimal power references and decision variables for distribution generation units, thereby enhancing the overall performance of the system. Finally, Wu et al. (2022) have conducted a study wherein they have proposed an economic model predictive

control strategy to achieve optimal control of an integrated energy system. The researchers have designed a zone tracking approach for building temperature regulation, with the objective of enhancing the operation of the system. The study findings suggest that the proposed zone tracking method significantly improves the overall performance of the integrated energy system, particularly in terms of meeting customized requirements.

The articles cited in this study are recent publications in esteemed journals, highlighting the significance of energy management systems for MGs. The predominant techniques employed in these works are rule-based and optimization-based methods. Rule-based approaches have the advantage of being easy to implement with low computational costs, but they require expertise in control systems to define the appropriate rules. The vast number of possible rule combinations can also result in varying outcomes. On the other hand, optimization-based techniques, particularly those applied to the MPC layer, are computationally expensive and often studied in isolation.

1.2 Contributions and objectives of the study

Approaches aimed at improving control strategies are typically employed at the MPC level for regulating the entire system or at the reference signal generator level to provide signals to the controller. Regardless of the application, the system is always updated based on real-time information from the microgrid, meaning that the controller reads MG variables to modify system conditions.

The impetus for undertaking this study stems from a recognized void in the extant literature pertaining to the management of microgrids. This lacuna is particularly conspicuous, given the scant attention afforded by existing research to the nuanced management of microgrids accommodating diverse load profiles throughout the weekly cycle, or to energy generation systems characterized by intermittent power output, where significant fluctuations occur between days of high and low demand. Furthermore, there exists a notable dearth of scholarly works addressing microgrid management systems that concurrently integrate three pivotal components: distinct energy storage devices, load profiles, and tariff pricing strategies. In light of these considerations, our overarching aim is to elucidate the technical and economic advantages engendered by the proposed approach within the realm of microgrid management.

That said, the principal contributions of this study are as follows:

- Propose a management model to address non-scheduled load systems in microgrids equipped with different types of energy storage systems, taking into account various energy market policies. The model comes in two variants: deterministic and stochastic, both aimed at gaining technical and economic advantages for the microgrid.

- Compare the proposed model with benchmark models and identify the advantages it offers over the models already enhanced in the literature.

As for the objectives of this work, the main one is to test a model with weighted parameters of two variants — deterministic and stochastic — for the management of grid-connected microgrids in specific cases: different types of loads, different tariff policies, and different energy storage systems.

To achieve this, some specific objectives are attained:

- To model mathematically the microgrid's wind and photovoltaic sources, load system, and electrical energy storage system, since this endeavor is predicated upon simulations of the microgrid system rather than relying solely on bench testing or empirical observations.

- To model mathematically the MPC controller.

- To estimate the parameters used in the mathematical equations of the power generation system as well as the control system based on manufacturers' datasheets.

- To present, explain, and evaluate the proposed model.

- To outline the scenarios in which the model will be implemented.

- To obtain the results from the proposed model and compare them to those from benchmark models enhanced in the literature.

1.3 Structure of the document

The present thesis is structured as follows: chapter 2 provides a detailed mathematical modeling of the renewable sources that are part of the microgrid, while chapter 3 outlines the microgrid energy storage system. Chapter 4 addresses the modeling of the MPC, and chapter 5 the microgrid structure, including the system control loop and the proposed research model. Chapter 6 describes a case study conducted to validate the proposed model, and chapter 7 provides a brief presentation of the benchmark models used for the proposed model valida-

tion. Chapter 8 presents and discusses the obtained results and, finally, chapter 9 presents concluding remarks and observations on the study.

2 Energy generating system: renewable sources

EGS is composed of various renewable sources of energy that have the capacity to generate electricity by utilizing resources that are replenished naturally within a human timescale. In contrast to the sources based on fossil fuels, the renewable sources have a higher potential to be eco-friendly and competitive in the market due to their minimal carbon emission into the atmosphere. Additionally, these sources are provided by nature free of cost, which makes them more cost-effective than the traditional sources of energy.

Numerous renewable energy systems are available that differ in their energy conversion resource. The names of these systems are indicative of the resources they utilize. For instance, hydropower depends on the gravitational energy that is present in the water flow, which is then converted into electrical energy. Wind and solar sources, on the other hand, utilize the wind and sunlight respectively to generate electricity. In this way, these systems harness natural resources to produce sustainable and eco-friendly energy.

The rise in global temperatures over the past few years has prompted countries to seek out alternative energy sources that emit fewer greenhouse gases. However, while clean energy is a priority, cost-effective electricity production is also a concern for owners. Hence, these sources must be carefully located in strategic areas. Hydroelectric power plants, for instance, necessitate specific conditions such as fast-flowing rivers, rugged terrain, and a consistent rainfall pattern to ensure continuity in electricity generation. In contrast, wind and solar farms rely on more flexible terrain characteristics, in addition to the abundant availability of wind and sunlight respectively.

Energy derived from wind and solar technology has witnessed a significant surge worldwide in recent years, surpassing the growth rate of other renewables. The production of electricity from hydropower has tripled since the 1970s, while the use of wind power has increased by approximately 1300% since the early 2000s. Additionally, solar photovoltaic technology has experienced an astonishing 17,000% increase in usage worldwide (ENERGY AGENCY, 2021). The available data serves as an indication of the enormous potential for wind and photovoltaic energy worldwide, and also reflects a growing interest in implementing global energy change.

2.1 Wind energy

The kinetic energy inherent in the movement of air may be utilized to generate electrical power. This process is facilitated by wind turbines, which are devoid of carbon dioxide emissions, rendering it a sustainable and ecologically sound energy source. Additionally, with the decline in wind technology expenditures, there has been a commensurate increase in the generation of electricity through both centralized and distributed wind energy production. Consequently, wind power has emerged as a prime focal point for multiple research investigations within the academic domain.

2.1.1   The wind turbine

The three-blade wind turbine is the most used machine for the energy conversion. When the wind blows through the blades, part of its energy is transmitted to the turbine, which, attached to a generator, turns and generates electric power. The efficiency of the energy conversion tends to increase according to the number of blades of the turbine, the higher the number of blades, the higher the efficiency; however, the investment cost also increases in line with the number of blades. The cost-efficiency rate shows that the three-blade turbine reaches a balance between high conversion efficiency and low investment cost, therefore, the ideal machine to be traded.

The process by which wind turbines convert kinetic energy derived from wind into electrical energy is accomplished through a multifaceted mechanical and electrical procedure. The aerofoil-like blades of the turbine enable wind to cause the rotor to revolve, which in turn rotates a shaft linked to a generator that generates electrical energy. The rotational velocity of the blades is contingent on the wind speed, and the rotor blades are formulated to rotate at a minimum speed, which is the point when the turbine starts producing electricity. The blades of the turbine continue to generate electricity until they attain a maximum speed, at which juncture, the turbine disengages to forestall harm due to high winds.

The entire process is supervised by a computerized system that monitors the wind velocity and direction, blade position, and electrical output. This system guarantees that the turbine operates in an efficient and safe manner, while concurrently maximizing the amount of electricity produced.

The predominant application of wind turbines has been in centralized energy generation. Such deployment entails the integration of multiple turbines in a wind farm to produce significant quantities of energy that are funneled to a substation, which subsequently interfaces with

the national electric grid. Thus, this paradigm represents a large-scale energy production process, wherein the energy source is geographically remote from the consumer. Although this model is the dominant mode of wind turbine deployment in the energy market, there are alternative configurations, referred to as decentralized, that leverage these energy conversion machines to generate electricity in proximity to the load point. While such arrangements are less common, they are often employed in prototypes utilized for academic research initiatives.

Recent works have been using wind sources in studies on microgrids (FATHY, 2023; HEIDARY; GHEISARNEJAD; KHOOBAN, 2023; HU et al., 2022; SAHRI et al., 2023; ZHU et al., 2023) reinforcing the importance of such topic for the scientific community. Many of them address technical and economic aspects of wind sources using analytical methods to estimate the active and reactive power of wind turbines. Thus, especially in studies that simulate the operation of a wind turbine, it is desirable to calculate the power supplied by such equipment.

2.1.2 Wind power equation modeling

As per the prevailing academic scholarship, the quantification of the electrical power output supplied by a wind turbine is accomplished through the employment of the Two Parameter Model, commonly referred to as eq. **Erro! Fonte de referência não encontrada.**. This modeling approach is extensively employed within the academic community for the purposes of research and analysis (BILENDO et al., 2023; FAHIM et al., 2022; HEIDARY; GHEISARNEJAD; KHOOBAN, 2023; MAGESH; DEVI; LAKSHMANAN, 2022).

$$P_{wind} = \frac{1}{2} C_p A_r \rho v^3 \qquad \text{2-1}$$

where P_{wind} is the electric power generated by the turbine (W), C_p is the power coefficient, A_r is the area swept by the turbine blades (m²), ρ is the air density (kg/m³), and v is the wind speed that crosses the turbine area (m/s).

The area swept by the blades is calculated by:

$$A_r = \frac{\pi d^2}{4} \qquad \text{2-2}$$

where d is twice the length of the turbine blades (m).

This equation is derived from the Bernoulli equation, and the modeling that results in

eq. $P_{wind} = \frac{1}{2} C_p A_r \rho v^3$ 2-1 can be seen in (CARVALHO; GUARDIA; MARANGON LIMA, 2019) .

The moment when the wind speed attains the turbine cut-in speed represents the point at which the inertia of the blades is overcome and the generation of electrical power commences. The production of electrical energy progressively increases until the rated power of the turbine is reached at the rated speed. Consequently, if the power generated by the wind augments from the cut-in speed until it attains the turbine rated power, the output remains constant despite any further increase in wind speed until the turbine cut-out speed is reached. A graphical representation of the power output of wind turbines as a function of wind speed is depicted in FIGURE 1, highlighting the critical turbine cut-in, cut-out, and rated speeds.

FIGURE 1 - TURBINE POWER VS. WIND SPEED
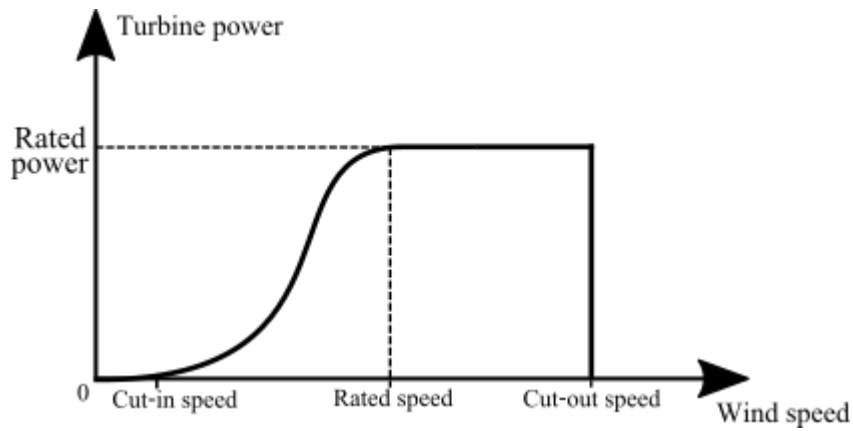
Therefore, the equation to calculate the turbine power changes from eqs.

$$P_{wind} = \frac{1}{2} C_p A_r \rho v^3$$

2-1 to

$$P_w = \begin{cases} 0 & \text{if } v < v_{cut-in} \\ P_{wind} & \text{if } v_{cut-in} \leq v \leq v_r \\ P_{wind\_rated} & \text{if } v_r \leq v \leq v_{cut-out} \\ 0 & \text{if } v > v_{cut-out} \end{cases}$$

2-3.

$$P_w = \begin{cases} 0 & \text{if } v < v_{cut-in} \\ P_{wind} & \text{if } v_{cut-in} \leq v \leq v_r \\ P_{wind\_rated} & \text{if } v_r \leq v \leq v_{cut-out} \\ 0 & \text{if } v > v_{cut-out} \end{cases}$$

2-3

where v_r, v_{cut-in}, and $v_{cut-out}$ are, respectively, the turbine rated speed (m/s), the cut-in speed (m/s), and the cut-out speed (m/s) and P_{wind_rated} is the turbine rated power (W).

2.1.3 The power coefficient (C_p)

One of the difficulties of calculating the turbine wind power by using eq.

$$P_{wind} = \frac{1}{2} C_p A_r \rho v^3$$

2-1 is to estimate the power coefficient — C_p — at each instant. The power coefficient is a dimensionless parameter used to describe the efficiency of a wind turbine. It represents the ratio of the actual power output of the turbine to the maximum possible power output, based on the amount of wind energy available at the turbine's location. In other words, it is the percentage of the available wind power that is being converted into electrical power. The power coefficient is an essential parameter in the turbine power equation, which relates the power output of the turbine to the wind speed, air density, rotor area, and power coefficient. The higher the power coefficient, the more efficiently the turbine can extract energy from the wind, resulting in a higher power output.

While the power coefficient of a wind turbine can be calculated through various methods, one common approach is to derive it from a wind speed regression analysis (AQUILA et al., 2016). This involves gathering data on the wind speed and power output of the turbine over a period of time, and then performing a regression analysis to determine the relationship between these two variables. By fitting a regression model to the data, the power coefficient can be estimated as the slope of the regression line, which represents the rate at which the power output of the turbine changes with respect to changes in wind speed. This method allows for the determination of the power coefficient under real-world operating conditions and can be used to optimize the performance of the turbine by identifying the wind speed range that yields the highest power output.

Given the length of the turbine blades, the air density, the output power, and the wind speed vectors, the power coefficient vector is found through a polynomial regression. Therefore, an equation that relates C_p and the wind speed is obtained.

$$C_p(v) = a_{(n)}v^n + a_{(n-1)}v^{n-1} + ... + a_0 \qquad \text{2-4}$$

where *a(n)*, *a(n-1)*, ..., *a₀* are the regression coefficients and *n* is the highest power of the equation, evaluated by the R-squared method.

The coefficient of determination — known as R-squared (R^2) — is a statistical measure that indicates how well a regression model fits the observed data. It is a value between 0 and 1, where 0 indicates that the model does not explain any of the variability in the data, and 1 indicates that the model perfectly explains all of the variability in the data. A high value of R-squared indicates that the regression model is a good fit for the data and that a large propor-

tion of the variation in the dependent variable can be explained by the independent variables in the model. On the other hand, a low value of R-squared suggests that the model is not a good fit for the data and that other factors may be influencing the dependent variable.

The coefficient of determination is calculated by squaring the correlation coefficient between the predicted values from the model and the actual observed values, and it represents the proportion of the total variation in the dependent variable that is explained by the independent variables in the model. In other words, it indicates the proportion of the variability in the data that is accounted for by the regression model.

R-squared can be calculated through eq. $R^2 = 1 - \dfrac{\sum (y_i - \hat{y}_i)^2}{\sum (y_i - \overline{y})^2}$ 2-5:

$$R^2 = 1 - \frac{\sum (y_i - \hat{y}_i)^2}{\sum (y_i - \overline{y})^2} \qquad \text{2-5}$$

where y_i, $\hat{y}_i$, and $\overline{y}_i$ are, respectively, the actual y value, the predicted y value, and the mean of y values.

A higher R^2 value indicates a better fit for the model.

2.1.4 The wind turbine used in the case study

In this work, a wind turbine is considered as part of an electric system generating power to a load complex. The market presents several types of wind technologies, whose parameters vary from model to model (WIND TURBINE MODELS, 2022), and a wind turbine with specific values of parameters is chosen to represent the wind system of this work. The Hummer H17.0-50 kW turbine with 17-meters-long blades and rated power of 50 kW is selected as the research's wind energy source. The choice of this turbine was based on its compliance with the specifications of the load data used in the study, as well as the availability of information provided by the manufacturer, which was used in modeling the wind energy production.

The power coefficient of this turbine is defined for a range of wind speed values. The power versus wind speed curve of the wind turbine used in the simulation and provided by the manufacturer is depicted in FIGURE 2. By utilizing this curve and the parameters of the turbine itself, one can derive the power coefficient curve — C_p — and subsequently estimate a regression curve for this parameter.

FIGURE 2 - POWER VS. WIND SPEED CURVE OF THE H17.0-50KW TURBINE
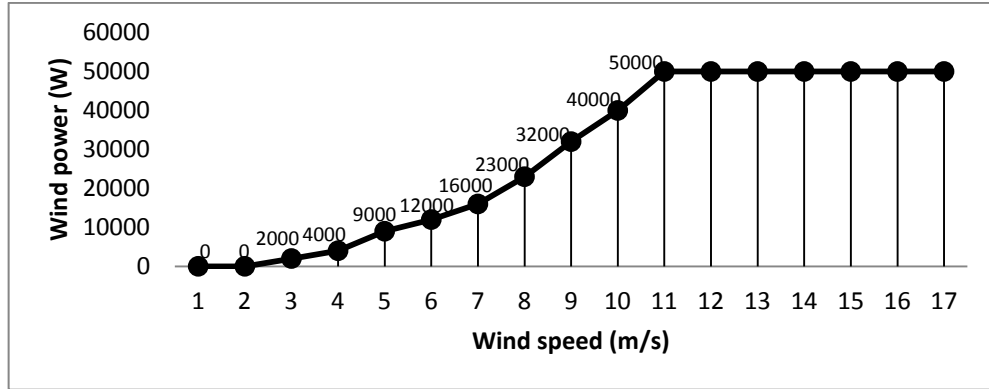
The C_p curve estimated by the regression process provides the following polynomial equation for wind speeds lower than 11 m/s:

$$C_p = -6.052 \times 10^{-4} v^6 + 2.182 \times 10^{-2} v^5 - 0.3129 v^4 + 2.264 v^3 - 8.591 v^2 + 15.655 v - 9.019 \qquad 2\text{-}6$$

Erro! Fonte de referência não encontrada. presents the C_p and the *Estimated C_p* curves. The C_p curve is derived from the graph shown in FIGURE 2 as well as from eq.

$$P_{wind} = \frac{1}{2} C_p A_r \rho v^3 \qquad 2\text{-}1,$$ while the *Estimated C_p* curve is obtained from the C_p regression

analysis.

FIGURE 3 - *Cp* AND *Cp* ESTIMATED THROUGH THE DATA REGRESSION PROCESS
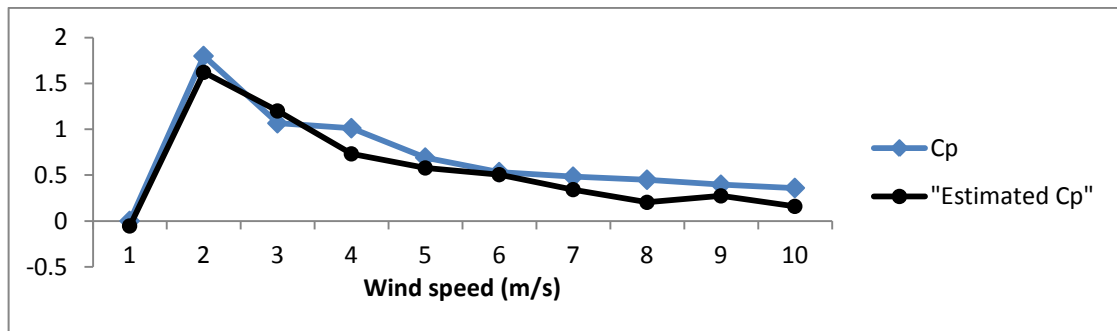
The regression analysis of the data enabled the derivation of equation 2, which specifies the wind power coefficient for each wind speed value. The regression R-squared value amounts to 0.950, indicating that 95% of the variation in the wind power coefficient can be explained by the linear relationship with the wind speed variable.

2.2 Solar power

2.2.1 The solar irradiance

The rays originating from the sun travel through vacuum until they reach the Earth. Upon reaching our planet and, therefore, coming into contact with the material medium, a por-

tion of the solar irradiance is reflected and absorbed, while another portion is transmitted to the surface. Thus, the solar irradiance that reaches the Earth's atmosphere can be decomposed in different ways, and some specific terms are addressed in this regard.

The solar irradiance that falls onto a surface is measured in a unit formed by four main components: the extraterrestrial, the direct normal, the diffuse, and the global horizontal irradiance. The extraterrestrial irradiance is the rate of incident energy per unit area on an imaginary horizontal plane located at the top of the atmosphere. The direct normal irradiance is defined as the rate of energy per unit area from the sun that strikes the surface perpendicularly. The diffuse irradiance is the rate of incident energy on a surface per unit area resulting from the scattering of direct solar beam by atmospheric constituents (molecules, particulate matter, clouds, etc.). Finally, the global horizontal irradiance is the total energy rate per unit area incident on a horizontal surface. The global irradiance is the sum of the diffuse and direct normal irradiance incident on a horizontal surface.

The integral of irradiance over time is defined as solar irradiation or accumulated incident radiant energy over a time interval. Note that although the terms irradiance and irradiation are cognate, they have distinct meanings. The difference between them is that the latter takes into account the energy accumulated over a unit of area and a certain period of time, such as over a day, for example, while the former considers only the power of solar light that falls on a unit of area, disregarding the accumulation of energy and the time in which it accumulates.

The solar irradiance is widely regarded as the primary and fundamental energy source that is utilized to instigate and perpetuate the photovoltaic effect. The photovoltaic effect, a physical phenomenon that involves the creation of a voltage and a current in a material, such as a semiconductor, upon exposure to electromagnetic radiation, is contingent upon the solar irradiance as its primary driving force. It is worth noting that the photovoltaic effect, being a crucial technology in the field of energy, has various applications, which span from the generation of electrical power to a wide range of other potential uses. Further elaboration on this subject will be provided in subsequent sections.

2.2.2 PV cell structure and photovoltaic effect

A photovoltaic cell is an electronic device capable of producing electricity from solar irradiation. They are built from semiconductor material, silicon being the most common component in their manufacture.

The process of doping, whereby materials lacking electrons, such as phosphorus, are incorporated into silicon to form the P layer of a photovoltaic cell, is a well-known technique. Conversely, materials that act as electron donors, like boron, are also added to silicon to produce the N layer of the device. Despite being adjacent, no electron flow occurs between these layers. However, an external conducting wire can be utilized to connect the two layers, enabling electric current to flow through the wire by way of electron transfer from the N layer to the P layer when sunlight photons fall on the cell. This is the photovoltaic effect, which is utilized by photovoltaic panels to generate electricity. In summary, the photovoltaic effect is a phenomenon that takes place when solar irradiance reaches a PV cell. The semiconductor material absorbs solar energy, leading to an excitation of electrons from the valence band to the conduction band. This excitation causes the flow of electrons, thereby creating a potential difference between the two sides of the photovoltaic cell.

In the context of photovoltaic technology, the quantity of solar irradiance that is assimilated by a photovoltaic cell is reliant on various factors, including the angle of incidence of the sunlight, the intrinsic material properties of the cell, and the wavelength of the incident light. As such, enhancing the design and orientation of photovoltaic cells can effectively enhance their performance in terms of converting solar irradiance into electrical energy. It is worth noting that photovoltaic cells can also be interconnected either in series or parallel configurations, leading to the formation of solar panels that exhibit augmented power output. These panels can subsequently be linked together to form an array, and upon the incidence of sunlight, a voltage is generated between the terminals of the array, ultimately leading to the generation of photovoltaic power.

Within academic discourse, the estimation of power output from solar panels has been a subject of interest, leading to several investigations in the literature. Numerous models have been proposed in scientific articles, taking into account various input parameters to estimate the output power of photovoltaic systems. Some of these models incorporate the surface area of the solar panels as an input variable (MELLOUK et al., 2019; SUN et al., 2022), while others require specific parameters under standard test conditions (HAN et al., 2021; KIM et al., 2022; RODRÍGUEZ-GÓMEZ et al., 2022; ROTAS et al., 2023). The next subsection discusses the equation used in this work to simulate the output power of the considered PV array.

2.2.3 PV power modeling

The equation proposed by Osterwald (OSTERWALD, 1986) is used in this research. This equation requests parameters that are tested in laboratories for the calculation of PV power; parameters of standard test conditions (STC) as shown in eq.

$$P_{pv} = P_{STC} \frac{G}{G_{STC}} \left[1 - \gamma (T_{cell} - 25) \right]$$

2-7.

$$P_{pv} = P_{STC} \frac{G}{G_{STC}} \left[1 - \gamma (T_{cell} - 25) \right] \qquad 2\text{-}7$$

where P_{pv} is the PV power provided by a solar panel (W), P_{STC} is the cell maximum power in STC (Standard Test Condition) (W), G_{STC} is the incident irradiance in standard test conditions (1000 W/m^2), G is the incident irradiance (W/m^2), γ is the coefficient of maximum power (1/ºC), and T_{cell} is the cell temperature (ºC).

The Osterwald's equation estimates the power of a solar panel based on parameters that are found in the manufacturer's datasheets, and this is one of the advantages of this equation since such manuals can be easily obtained on the websites of companies that build such panels.

$$P_{pv} = P_{STC} \frac{G}{G_{STC}} \left[1 - \gamma (T_{cell} - 25) \right]$$

Note, however, that eq. 2-7 only provides the power of one solar panel; however, solar panel arrays for high power generation often have hundreds or thousands of modules connected in series and/or in parallel. Therefore, to estimate the total

$$P_{pv} = P_{STC} \frac{G}{G_{STC}} \left[1 - \gamma (T_{cell} - 25) \right]$$

power generated by the PV array, eq. 2-7 is modified and

$$P_{pv} = P_{STC} \frac{G}{G_{STC}} \left[1 - \gamma (T_{cell} - 25) \right] N_{pv}$$

becomes eq. 2-8. In this equation, the N_{pv} parameter is added.

$$P_{pv} = P_{STC} \frac{G}{G_{STC}} \left[1 - \gamma (T_{cell} - 25) \right] N_{pv} \qquad 2\text{-}8$$

where N_{pv} is the number of PV panels connected in the array.

$$T_{cell} = T_{amb} + \frac{G}{G_{NOCT}} \left(NOCT - T_{amb,NOCT} \right)$$

The T_{cell} parameter is calculated using 2-9.

$$T_{cell} = T_{amb} + \frac{G}{G_{NOCT}} \left(NOCT - T_{amb,NOCT} \right) \qquad\qquad 2\text{-}9$$

where T_{amb} is the ambient temperature (ºC), G_{NOCT} is the irradiance in which the cell temperature is the NOCT (W/m^2), NOCT is the Normal Operating Cell Temperature (ºC), and $T_{amb,NOCT}$ is considered to be equal to 25 ºC.

Therefore, once the parameters of the wind and the solar power equations are defined and the wind speed and the solar irradiance data are collected, the power of each renewable source can be estimated.

2.2.4   The solar panel used in the case study

The parameters of the solar panel for estimating the photovoltaic power are obtained from the manufacturer's datasheet. In this work, a High Power Bifacial Poly Perc. Module 400 W ~ 425 W panel manufactured by the Canadian Solar is used as a model, and a set of 100 solar panels completes the module array that is considered in this study. According to the Canadian Solar datasheet shown in appendix A of this document and found in (CANADIAN SOLAR, 2023), the parameters for this type of module are $P_{stc} = 400W$, $G_{NOCT} = 800$ W/m^2, NOCT = 41 ºC, and $\gamma = 0.0036$.

2.3 Main considerations

The purpose of this chapter was to introduce concepts related to solar and wind energy that constitute the energy generation system in this study. The chapter outlined the mathematical modeling of such devices as an integral part of the overall microgrid modeling process.

3 Energy storage system: battery and ultra-capacitor

As energy storage systems, batteries have become a highly promising technology for delivering a range of services in stationary applications across residential, commercial, and industrial sectors. These services can be broadly categorized into several types: end-user energy management services, which include power quality and reliability; services for renewable energy applications, such as renewable time-shifting and renewable firming; ancillary services, such as load following and frequency regulation; and bulk energy services, such as energy arbitrage and peak shaving (SHABANI et al., 2023).

In addition to batteries, ultra-capacitors have also garnered significant interest as a solution for start-stop energy system applications in industries, including heavy-duty trucks, space power, armored cars, and transit buses. These devices are designed to rapidly capture and deliver power, and have been developed to enhance energy efficiency, reduce fuel consumption, and decrease carbon dioxide emissions in pulse power and energy-saving applications.

In this work, a system composed by a battery and an ultra-capacitor is taken as the ESS. The modeling of this system that considers the electrical circuit of the battery and the UC is shown in this section. It is an established fact that the ESS is capable of operating in two modes, acting either as a load by consuming electricity from the power grid or as a power generation system by providing energy to the grid. To ensure precision in modeling the ESS, both modes of operation should be incorporated; however, the modeling of the storage system power becomes excessively intricate when representing both ESS behaviors, and thus only one mode is taken into account in this study. Specifically, this research focuses on the scenario where the ESS supplies energy to the MG and this is mathematically modeled in the subsequent subsection.

3.1 Battery system modeling

Producers of batteries are engaged in ongoing experimentation with novel chemical compositions, in pursuit of the objective of crafting batteries that are less expensive, more compact, less weighty, and more potent, while simultaneously exhibiting greater retention capacity (ABU et al., 2023). Due to its favorable characteristics with regard to energy efficiency, power and energy density, as well as longevity, the lithium-ion battery is widely recognized as a highly promising technology for battery energy storage system (HOW et al., 2020).

In 1991, the initial usage of lithium-ion batteries was recorded by Sony, a multinational corporation (CHEN et al., 2009). Two decades later, the production of these batteries has escalated to a level of two billion cells annually, which are employed in a variety of applications (GALLO et al., 2016).

The constituents of lithium-ion batteries, including the cathode, anode, separator, and electrolyte, collaboratively enable the transference of lithium ions via the separator from the cathode to the anode and vice versa during the charge/discharge cycle. Various materials, such as metallic lithium, graphitic carbon, hard carbon, synthetic graphite, lithium titanate, tin-based alloys, and silicon-based elements, are currently employed in the fabrication of anodes (FAN et al., 2019). The cathodes that are currently utilized in commercial applications consist of recently introduced materials, namely lithium nickel manganese cobalt oxide, lithium cobalt oxide, lithium nickel cobalt aluminum oxide, and lithium iron phosphate (LI; ERICKSON; MANTHIRAM, 2020; MANTHIRAM, 2020).

A battery can exhibit the states of charging and discharging. During the discharge state, the migration of positively charged lithium ions (Li^+) occurs from the negative anode towards the positive cathode. This movement transpires by means of traversing the electrolyte until the point where the positive electrode is reached, where the lithium ions are deposited. Meanwhile, the electrons travel from the anode to the cathode.

When a lithium-ion battery is subjected to the charging process, the opposite process ensues. Specifically, the lithium ions undergo migration from the cathode to the anode, while the electrons move from the anode to the cathode. The consistent movement of lithium ions from one electrode to another sustains a continuous flow of electrons, thereby providing the energy required to power the device. Since this process can be repeated numerous times, the lithium-ion battery is deemed rechargeable.

For the purpose of simulating the microgrid, it is of interest to analyze the circuit of the battery system, and thus, such a system must be mathematically modeled.

For this purpose, consider FIGURE 4. It depicts the electrical circuit of a battery with a voltage source E, an equivalent resistance $R_{p(bat)}$ in parallel with a capacitor representing the parasitic capacitance C_{bat} of the system, and an equivalent resistance $R_{s(bat)}$ in series with the load that is connected to the circuit terminals. Furthermore, note that V_{Cbat} and i_{Cbat} denote, respectively, the voltage and current flowing through the capacitor of the battery, whereas V_{bat} and i_{bat} represent the voltage and current supplied to the load.

FIGURE 4 - BATTERY ELECTRICAL CIRCUIT
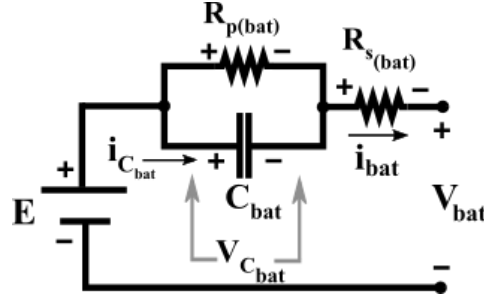
The power that the battery delivers, as modeled in Appendix A of this document, can be determined through equation

$$P_{bat} = V_{bat}i_{bat} = E\,i_{bat} + R_{p(bat)}i_{Cbat}i_{bat} - (R_{p(bat)} + R_{s(bat)})i^2_{bat} \quad 3\text{-}1.$$

$$P_{bat} = V_{bat}i_{bat} = E\,i_{bat} + R_{p(bat)}i_{Cbat}i_{bat} - (R_{p(bat)} + R_{s(bat)})i^2_{bat} \qquad 3\text{-}1$$

3.2 Ultra-capacitor system modeling

There exist various alternatives to batteries, among which lies the ultra-capacitor, a device of particular interest. These specialized capacitors possess a large capacitance and amalgamate characteristics of batteries and capacitors into one singular device. Over the past few years, ultra-capacitors have undergone significant maturation and have displayed potential to advance energy storage systems. As opposed to conventional batteries or capacitors, ultra-capacitors exhibit a considerably shorter charging time and are capable of discharging in a similar fashion to standard batteries. Additionally, they are lightweight and environmentally benign in comparison (GAUTHAM PRASAD et al., 2019).

Traditional capacitors store energy by means of electron transfer from one electrode to another. In contrast, ultra-capacitors that employ carbon materials boast a significantly greater surface area. This characteristic enables the utilization of a phenomenon termed as the electric double layer to facilitate charge storage. Despite being subject to the same capacitance equations, ultra- and electrolytic capacitors differ in their capacitance capabilities. Ultra-capacitors are capable of achieving higher capacitance owing to their utilization of a thinner dielectric and greater surface area of electrodes. This unique attribute also allows for a power density superior to that of batteries and an energy density surpassing that of traditional capacitors.

In ultra-capacitors, charges are stored electrostatically without any transfer. When a voltage is applied across the terminals of an UC, an electric field is generated in the electrolyte, causing its polarization. This, in turn, results in the diffusion of ions through the dielectric to the porous electrodes of opposite charges. Consequently, an electric double layer is formed at each electrode, reducing the distance between electrodes and increasing the surface

area of the electrode. The energy storage capacity of UCs depends on the active material employed in the electrolyte, the surface area of the electrode, and the utilization rate of micro-holes present in the porous electrode.

According to Stepanov (2006), ultra-capacitors have the following advantages:

- rapid recharge capability within minutes;
- wider temperature range versus batteries;
- low degradation after 100 000 cycles;
- environment safety;
- high efficiency (above 95%);

Disadvantages:

- high price;
- energy density lower that in batteries;
- voltage depends on a degree of charge.

Similar to battery systems, ultra-capacitors can be mathematically modeled for the purpose of MG simulation. In this regard, the equivalent electrical circuit depicted in FIGURE 5 is used.

FIGURE 5 - UC ELECTRICAL CIRCUIT
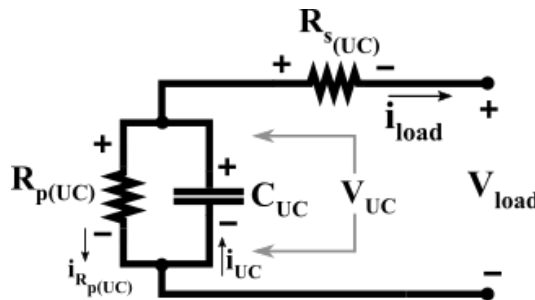
This circuit model has been thoroughly investigated in a prior study (SPYKER, 2000) and subsequently applied in several recent publications (HELSETH, 2022; SATPATHY; DEBBARMA; BHATTACHARYYA, 2019; SHABANI et al., 2023). It is worth noting that the UC electrical circuit model shares similarities with that of the battery; however, the UC one does not contain a voltage source. Instead, it comprises of a capacitor with a capacitance of C_{UC} that is connected in parallel with an equivalent resistor with a resistance of $R_{p(UC)}$, and this branch of the circuit is connected in series with an equivalent resistor of resistance $R_{s(UC)}$. The current that traverses the capacitor is represented as i_{UC}, the current that flows through the parallel resistor is represented as i_{RpUC}, and the current that is supplied to the load is represent-

ed as i_{load}. Furthermore, the voltage across the capacitor is denoted as V_{UC}, and the voltage supplied to the load is V_{load}.

The power delivered by an ultracapacitor is modeled in Appendix A, Section I of this document. Through this modeling, it is found that the UC power equation is given by:

$$P_{UC} = R_{p(UC)}i^2_{UC} - R_{p(UC)}i_{load}i_{UC} \qquad \text{3-2}$$

3.3 ESS power linearization

According to eqs. $P_{bat} = V_{bat}i_{bat} = E\,i_{bat} + R_{p(bat)}i_{Cbat}i_{bat} - (R_{p(bat)} + R_{s(bat)})i^2_{bat}$ 3-1 and

$P_{UC} = R_{p(UC)}i^2_{UC} - R_{p(UC)}i_{load}i_{UC}$ 3-2, it can be observed that the power output of energy storage systems is calculated based on the square of the current, indicating a non-linear relationship. To enable the integration of a linear model into the state space model, it is necessary to perform a linearization of the power output of the energy storage system.

In order to achieve the linearization, an operating range is established for the input variables, and their values are constrained within the defined limits. Following the determination of these parameters, equations that represent the system output are partially derived with respect to the state variables.

Assuming that C is the Jacobian output matrix, g_1, g_2, ..., g_n are the equations for the output variables, and τ_1, τ_2, ..., τ_n are the system state variables, the linearization is performed in accordance with the following method.

$$C = \begin{bmatrix} \left.\dfrac{\partial g_1}{\partial \tau_1}\right|_{\tau_1=\tau_{1,1}} & \cdots & \left.\dfrac{\partial g_1}{\partial \tau_n}\right|_{\tau_n=\tau_{1,n}} \\ \vdots & \ddots & \vdots \\ \left.\dfrac{\partial g_n}{\partial \tau_1}\right|_{\tau_1=\tau_{n,1}} & \cdots & \left.\dfrac{\partial g_n}{\partial \tau_n}\right|_{\tau_n=\tau_{n,n}} \end{bmatrix}$$

where the terms $\tau_{1,1}$, $\tau_{1,n}$, , $\tau_{n,1}$, ... $\tau_{n,n}$ are constant values that are specified.

To modify eqs. $P_{bat} = V_{bat}i_{bat} = E\,i_{bat} + R_{p(bat)}i_{Cbat}i_{bat} - (R_{p(bat)} + R_{s(bat)})i^2_{bat}$ 3-1 and

$P_{UC} = R_{p(UC)}i^2_{UC} - R_{p(UC)}i_{load}i_{UC}$ 3-2, the state variables i_{bat} and i_C are substituted with $\tau_{1(bat)}$ and $\tau_{2(bat)}$; i_{bat} and i_C are replaced with $\tau_{1(UC)}$ and $\tau_{2(UC)}$, respectively. Afterwards, the equations are rephrased and written in a new form.

$$g_{bat}\left(\tau_{1(bat)}, \tau_{2(bat)}\right) = E\tau_{1(bat)} + R_{p(bat)}\tau_{2(bat)}\tau_{1(bat)} - \left(R_{p(bat)}R_{s(bat)}\right)\tau^2_{1(bat)} \qquad \text{3-3}$$

$$g_{UC}\left(\tau_{1(UC)}, \tau_{2(UC)}\right) = R_{p(UC)}\tau^2_{2(UC)} - R_{p(UC)}\tau_{1(UC)}\tau_{2(UC)} \qquad \text{3-4}$$

Utilizing the principles introduced in the linearization process of matrix C, we find:

$$C_{(bat)} = \left[E + R_{p(bat)}\tau_{2(bat)} - 2R_{p(bat)}R_{s(bat)}\tau_{1(bat)} \quad R_{p(bat)}\tau_{1(bat)} \quad 0\right] \qquad \text{3-5}$$

$$C_{(UC)} = \left[-R_{p(UC)}\tau_{2(UC)} \quad 2R_{p(UC)}\tau_{2(UC)} - R_{p(UC)}\tau_{1(UC)} \quad 0\right] \qquad \text{3-6}$$

Upon equating $g_{bat}\left(\tau_{1(bat)}, \tau_{2(bat)}\right) = E\tau_{1(bat)} + R_{p(bat)}\tau_{2(bat)}\tau_{1(bat)} - \left(R_{p(bat)}R_{s(bat)}\right)\tau^2_{1(bat)}$ 3-3

and $g_{UC}\left(\tau_{1(UC)}, \tau_{2(UC)}\right) = R_{p(UC)}\tau^2_{2(UC)} - R_{p(UC)}\tau_{1(UC)}\tau_{2(UC)}$ 3-4

$C_{(bat)} = \left[E + R_{p(bat)}\tau_{2(bat)} - 2R_{p(bat)}R_{s(bat)}\tau_{1(bat)} \quad R_{p(bat)}\tau_{1(bat)} \quad 0\right]$ 3-5 to zero, a correlation is

discovered between the system's state variables.

$$\tau_{2(bat)} = \tau_{1(bat)}\frac{(R_{p(bat)} + R_{s(bat)})}{R_{p(bat)}} - \frac{E}{R_{p(bat)}} \qquad \text{3-7}$$

$$\tau_{2(UC)} = \tau_{1(UC)} \qquad \text{3-8}$$

If a variable is defined, the other variable can be determined by utilizing eqs.

$\tau_{2(bat)} = \tau_{1(bat)}\frac{(R_{p(bat)} + R_{s(bat)})}{R_{p(bat)}} - \frac{E}{R_{p(bat)}}$ 3-7 and $\tau_{2(UC)} = \tau_{1(UC)}$ 3-8. Step and ramp inputs are

utilized to investigate the response of the output power with respect to the current. A range of

values for $\tau_{1(bat)}$ and $\tau_{1(UC)}$ and, along with their corresponding τ_2 values, were assessed using

the RMSE (Root Mean Squared Error) method, as follows:

$$\sqrt{\frac{1}{n}\sum_{j=1}^{n}\left(y_j - \bar{y}_j\right)^2}$$

where "n" represents the number of samples or observations within the dataset. Additionally,

the terms y_j and $\bar{y}_j$ correspond to the actual and predicted values of the variable power, re-

spectively.

RMSE measures the proximity of data points to the best-fit line derived from eqs.

$P_{bat} = V_{bat}i_{bat} = E\,i_{bat} + R_{p(bat)}i_{Cbat}i_{bat} - (R_{p(bat)} + R_{s(bat)})i^2_{bat}$ 3-1 and

$P_{UC} = R_{p(UC)}i^2_{UC} - R_{p(UC)}i_{load}i_{UC}$ 3-2. A smaller RMSE indicates a higher concentration of

data points around this line, making it necessary to obtain small RMSE values. The RMSE

values are provided for both step and ramp input cases, for each considered value of τ_1 and τ_2, as well as for each ESS device.

TABLE 1 - LINEARIZATION DATA

	τ_1	τ_2	Step input RMSE (x10³)	Ramp input RMSE (x10³)
Linearization of battery power	13,000	-15,570	55.265	35.284
	-12,000	-14,470	47.349	36.290
	-11,000	-13,370	46.647	42.521
	-10,500	-12,820	49.222	47.019
	-10,000	-12,270	53.445	52.138
	-9,000	-11,170	65.445	63.622
Linearization of UC power	615	615	2,490	205
	620	620	2,484	205
	655	655	2,445	205
	660	660	2,440	205

In the instance of the battery, the values $\tau_{1(bat)} = -12,000$ and $\tau_{2(bat)} = -14,470$ are selected. Similarly, for the ultra-capacitor, the values $\tau_{1(UC)} = \tau_{2(UC)} = 655$ are employed. The parameters are confined within the range limits of -3000 A $\leq i_{bat} \leq$ 3000 A and -1000 A $\leq i_{UC} \leq$ 1000 A.

FIGURE 6 provides a graphical representation of Table 1 - Linearization data. The bold black line denotes the actual power drawn or supplied by each Energy Storage System (ESS) device, which is determined by employing equations

$$P_{bat} = V_{bat}i_{bat} = E\,i_{bat} + R_{p(bat)}i_{Cbat}i_{bat} - (R_{p(bat)} + R_{s(bat)})i^2_{bat} \quad \text{3-1}$$

and

$$P_{UC} = R_{p(UC)}i^2_{UC} - R_{p(UC)}i_{load}i_{UC} \quad \text{3-2}$$

in relation to the current. The lines in various colors correspond to the linearized power values obtained from eqs.

$$g_{bat}\left(\tau_{1(bat)}, \tau_{2(bat)}\right) = E\tau_{1(bat)} + R_{p(bat)}\tau_{2(bat)}\tau_{1(bat)} - \left(R_{p(bat)}R_{s(bat)}\right)\tau^2_{1(bat)} \quad \text{3-3}$$

and

$$g_{UC}\left(\tau_{1(UC)}, \tau_{2(UC)}\right) = R_{p(UC)}\tau^2_{2(UC)} - R_{p(UC)}\tau_{1(UC)}\tau_{2(UC)} \quad \text{3-4},$$

which vary according to the different values of τ_1 and τ_2 presented in Table 1 - Linearization data. The step and ramp inputs are applied and depicted in the graphs.

FIGURE 6 - GRAPHS SHOWING THE ESS POWER LINEARIZATION PROCESS
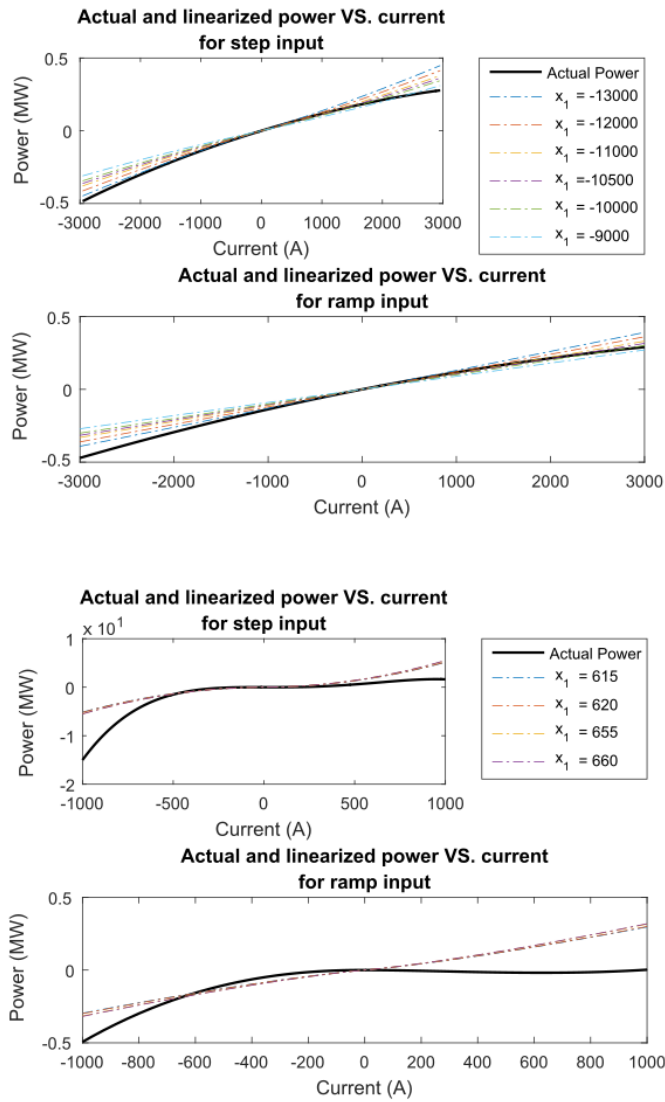
3.4 Main considerations

This chapter has been intended to present the concepts of batteries and ultra-capacitors, which are devices that constitute the energy storage system of this study. Furthermore, the chapter portrayed the mathematical modeling of these devices as an integral part of the entire microgrid modeling process.

4 MPC modeling

This section presents the control model that is employed in this work for microgrid management. All information regarding the content is derived from Camacho and Bordons (1999).

4.1 Introduction to model based on predictive control actions

Model Predictive Control encompasses a wide range of control methods that utilize a process model to minimize an objective function. These design approaches result in controllers with a similar structure and appropriate degrees of freedom. The fundamental concepts that underlie the predictive control family include:

- The utilization of a process model to forecast the process output at future time intervals (horizons).

- The determination of a control sequence that minimizes an objective function.

- The implementation of a receding strategy, whereby the horizon is continuously shifted towards the future at each instant, and involves the execution of the first computed control signal from the sequence at each iteration.

Predictive control is currently being widely used in various fields, not just limited to the process industry. It has been applied successfully in controlling different processes, ranging from robot manipulators to clinical anesthesia. Predictive control has also been used in the cement industry, drying towers, robot arms, and many other types of application since it presents a series of advantages such as:

- It is particularly attractive to staff with only a limited knowledge of control because the concepts are very intuitive and at the same time the tuning is relatively easy.

- This particular control method is very flexible and can be applied to a wide range of processes, even those with complicated dynamics such as long delay times, non-minimum phase, or unstable behavior. It is not limited to controlling simple processes and can handle various challenges that arise in more complex systems. Overall, this method is versatile and robust, making it an effective choice for controlling a diverse range of processes.

- It can handle multivariable systems without difficulty.

- It has built-in compensation for dead times.

- It naturally incorporates feed-forward control to counteract measurable disturbances.
- The resulting controller is a simple linear control law that is easy to implement.
- Among other examples.

The approach used in the controllers within the MPC family is defined by the following strategy, as illustrated in **Erro! Fonte de referência não encontrada.**

FIGURE 7 - MPC CONTROL ACTION
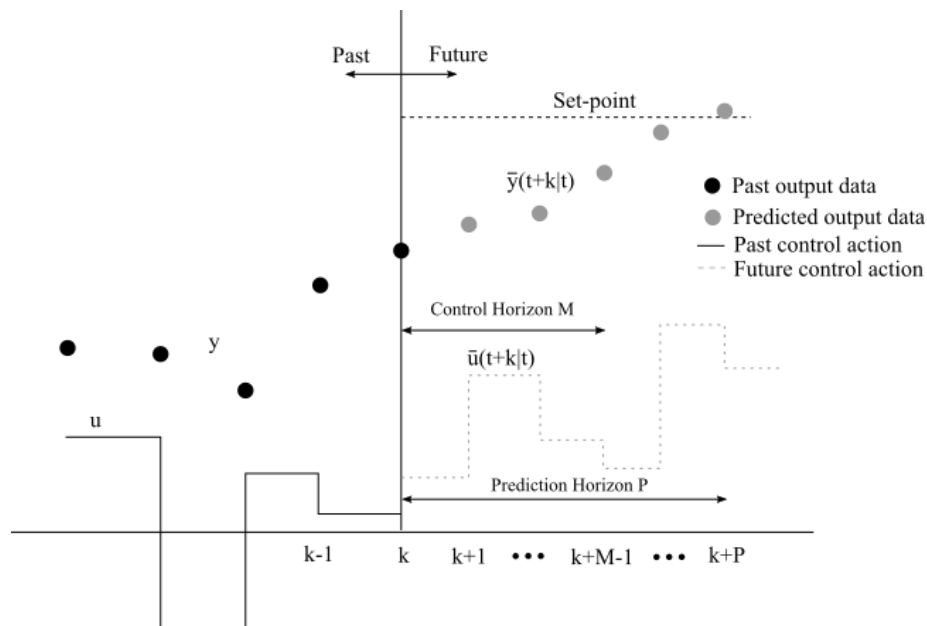
1. At every moment *t*, the process model is used to predict future outputs for a set time period, known as the prediction horizon. These forecasts, denoted as y(t+k|t) for k = 1 ... P, are dependent on previously known inputs and outputs up to time *t*, as well as the future control signals u(t+k|t), k = 0 ... P, which are computed and transmitted to the system. Note that y(t+k|t) means *k* steps from time *t*.

2. To control a process and keep it close to a desired trajectory, we can use model predictive control. This involves optimizing a cost function that measures the difference between the predicted output and the desired trajectory. This cost function typically has a quadratic form and includes the control effort.

3. The control system sends a control signal to the process based on the current state of the system. The control algorithm then predicts the future behavior of the system using a model, taking into account new information that becomes available over time. The algorithm repeats this process at each time step, updating its predictions and calculating a new control signal based on the updated in-

formation. This approach is known as the receding horizon concept, and it allows the control system to continuously adapt to changes in the system and optimize its performance over time.

To put the strategy of model predictive control into action, it is used the basic structure illustrated in FIGURE 8. The first step is to use a model that can predict the future outputs of the plant. This prediction is based on the past and present values of the plant and the proposed optimal future control actions. The second step is to calculate the optimal control actions using an optimizer that takes into account the cost function. The cost function is usually a quadratic function that takes into account the future tracking error and the control effort. The third step involves imposing any constraints on the system, such as physical or operational limitations. By using this approach, we can dynamically optimize control actions based on the predicted behavior of the plant and ensure that the system remains as close as possible to the desired trajectory while satisfying the system's constraints.

FIGURE 8 - BASIC STRUCTURE OF MPC
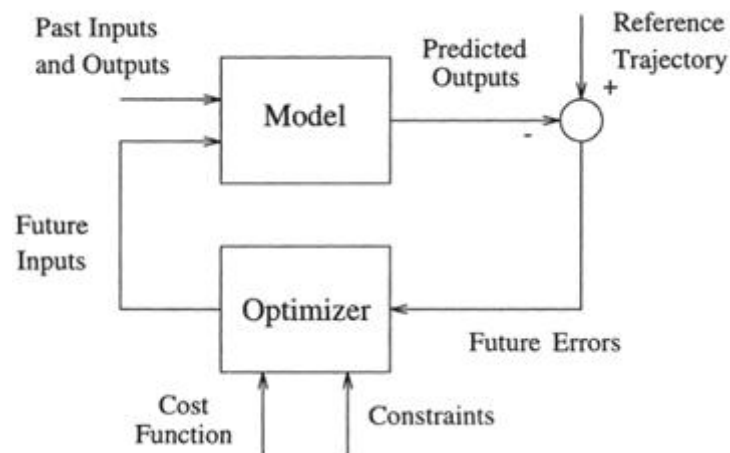
SOURCE: CAMACHO; BORDONS (1999).

Note on FIGURE 8 that the Future Errors signal is the result of subtracting the Reference Trajectory signal from the Prediction Outputs signal. The reference signal is the set-point established by the user or automated for control purposes and is the object of study in this research.

MPC or Model Predictive Control is a collection of control techniques that utilize future variable predictions to execute control actions. As per control theory principles, MPC makes predictions within the prediction horizon and takes control actions within the control horizon.

Model Predictive Control can be utilized in various industrial and engineering applications where precise control over a system is required. Some examples of cases where MPC can be used include:

- Chemical processes: in chemical processes, MPC can be used to regulate the temperature, pressure, and flow rates of different materials, ensuring that the chemical reactions proceed optimally.

- Power systems: in electrical power systems, MPC can be used to balance the load on the grid and manage the frequency of the electrical signal, helping to prevent blackouts or other power disturbances.

- Robotics: in robotics, MPC can be used to optimize the motion and path planning of robots, ensuring they operate efficiently and safely.

- Automotive industry: in the automotive industry, MPC can be used to control the engine and transmission of vehicles, ensuring optimal fuel efficiency and reduced emissions.

- Building automation: in building automation systems, MPC can be used to optimize energy consumption, regulating heating, cooling, and lighting to reduce energy waste and save costs.

Overall, MPC can be utilized in any application where there is a need for precise control over a dynamic system, and where there are constraints on the system that must be considered in the control strategy.

4.2 MPC and plant modeling

The MPC framework is designed to consider the variables that are present in the state space model. As a result, the aforementioned equations are expressed by means of this type of representation, which employs matrices to depict the power system model. Specifically, the discrete-time, time-invariant state space model for a linear system is portrayed in the following manner:

$$
\begin{aligned}
x(k+1) &= Ax(k) + Bu(k) \\
y(k) &= Cx(k) + Dr(k)
\end{aligned}
$$

4-1

where:

$$x = \begin{bmatrix} i_{bat} \\ i_c \\ i_{load} \\ i_{UC} \end{bmatrix} \quad \text{and} \quad u = \begin{bmatrix} i'_{bat} \\ i'_{UC} \end{bmatrix}$$

The apostrophe in i'_{bat} and i'_{UC} indicates the derivative of those parameters. The output is the grid power given by:

$$P_{grid}(k+1) = P_{bat}(k) + P_{UC}(k) + P_{total}(k) \qquad \text{4-2}$$

P_{total} represents the net power available in the system, obtained by subtracting the power demand of the load from the total power supplied by the sources, that is,

$$P_{total}(k) = P_w(k) + P_{pv}(k) - P_{load}(k) \qquad \text{4-3}$$

The total power is represented in state space model as r(k). Note that P_{total} represents an uncontrolled input to the system; that is, this variable signifies the noise in the modeled framework.

Upon examination of eq. $P_{grid}(k+1) = P_{bat}(k) + P_{UC}(k) + P_{total}(k)$ 4-2, it can be observed that when the grid power value is positive, it indicates that power is being delivered to the grid. Conversely, when the grid power value is negative, it indicates that power is being drawn from the grid to charge the ESS. Moreover, when the grid power value is zero, it indicates that the total power output from both the energy sources and the energy storage system is equal to the power demanded by the load.

The state space model used for control system modeling can be expressed by the following set of matrices, where the values of *n*, *p*, and *q* are determined by the number of rows and columns of matrix *A*, of matrix *B*, and of matrix *C*, respectively. For the specific work being referenced here, the values of *n*, *p*, and *q* are 4, 2, and 1, respectively.

$$\underbrace{\begin{bmatrix} i'_{bat} \\ i'_C \\ i'_{load} \\ i'_{UC} \end{bmatrix}}_{x'} = \underbrace{\begin{bmatrix} 0 & 0 & 0 & 0 \\ 0 & \dfrac{-1}{R_{p(bat)}} & 0 & 0 \\ 0 & 0 & 0 & \dfrac{-1}{R_{p(UC)}C_{UC}} \\ 0 & 0 & 0 & 0 \end{bmatrix}_{n\times n}}_{A} x + \underbrace{\begin{bmatrix} 1 & 0 \\ 1 & 0 \\ 0 & 1 \\ 0 & 1 \end{bmatrix}_{n\times p}}_{B} u$$

$$y = \underbrace{\begin{bmatrix} E + R_{p(bat)}x_{2,0(bat)} - 2(R_{p(bat)} + R_{s(bat)})x_{1,0(bat)} \\ R_{p(bat)}x_{1,0(bat)} \\ R_{p(UC)}x_{2,0(UC)} - 2(R_{p(UC)} + R_{s(UC)})x_{1,0(UC)} \\ R_{p(UC)}x_{1,0(UC)} \end{bmatrix}^{T}}_{C} x + \underbrace{[1]P_{total}(k)}_{D}$$

MPC is a collection of control techniques that utilize future variable predictions to execute control actions. As per control theory principles, MPC makes predictions within the prediction horizon (m_p) and takes control actions within the control horizon (m_c).

In this work, $m_p = m_c = 5$.

$$x(k+1) = Ax(k) + Bu(k)$$

Eq. $\quad y(k) = Cx(k) + Dr(k) \quad$ 4-1 provides output $y(k)$, which is used to derive future predictions such as $y(k+1)$, $y(k+2)$, and so on up to $y(k+m_c)$. These future forecasts are estimated according to the prediction equation shown in Appendix B, Section II of this document.

The output vector y is determined by employing eq. $\quad y = G_y x(k) + \theta_y u + Kr \quad$ 4-4, while the space state vector **x** is updated in accordance with eq. $\mathbf{x} = G_x x(k) + \theta_x u$ 4-5. The parameters of the equations are presented in Appendix B, Section II of this document.

$$y = G_y x(k) + \theta_y u + Kr \qquad \text{4-4}$$

$$\mathbf{x} = G_x x(k) + \theta_x u \qquad \text{4-5}$$

The objective function of the MPC is designed to reduce the discrepancy between the actual output and the desired reference signal. This function utilizes a quadratic function in the controller model to effectively perform this task. In general, the MPC function takes into account the difference between the reference signal and the output signal, and punishes the input signal accordingly, as illustrated in eq. $\quad J = \left(y - y_{ref}\right)^{T} W_y \left(y - y_{ref}\right) + u^{T}W_u u \quad$ 4-6.

$$J = \left(y - y_{ref} \right)^T W_y \left(y - y_{ref} \right) + u^T W_u u \qquad \text{4-6}$$

where y_{ref}, W_y, and W_u are assigned in Appendix B, Section II.

The diagonal values of W_u and W_y, denoted as w_u and w_y, were established through a trial-and-error process. Employing this method, we opted for the values $w_u = 1$ and $w_y = 0.01$.

The controller imposes limitations on both the current and the SOC (State of Charge) of the energy storage system. These restrictions can be mathematically expressed in terms of inequality constraints, as represented by matrices.

$$IU \leq U_{max} \quad and \quad -IU \leq -U_{max} \qquad \text{4-7}$$

where I is the identity matrix. Vector U is presented in Appendix B, Section II.

The restriction of the SOC variable is given as:

$$SOC_{min} \leq SOC - \frac{QX}{Q_r} \leq SOC_{max} \qquad \text{4-8}$$

This inequality can be derived by taking into account two additional inequalities:

$$SOC - \frac{QX}{Q_r} \geq SOC_{min} \quad and \quad SOC - \frac{QX}{Q_r} \leq SOC_{max} \qquad \text{4-9}$$

Developing both equations and assuming that X has been calculated through eq.

$$Q\theta_x U \leq -QG_x x(k) + Q_r \left(SOC - SOC_{min} \right) \quad and \quad -Q\theta_x U \leq QG_x x(k) + Q_r \left(SOC_{max} - SOC \right) \quad \text{4-10.}$$

$$Q\theta_x U \leq -QG_x x(k) + Q_r \left(SOC - SOC_{min} \right) \quad and \quad -Q\theta_x U \leq QG_x x(k) + Q_r \left(SOC_{max} - SOC \right) \quad \text{4-10}$$

The variables q_{rbat} and q_{rUC} represent the charge capacity of the battery and ultra-capacitor, respectively, and are measured in ampere-hours (Ah). The variables $soc_{min(bat)}$ and $soc_{min(UC)}$ indicate the minimum level to which the battery and ultra-capacitor can be charged, respectively, as a proportion of their total capacity. The variables $soc_{max(bat)}$ and $soc_{max(UC)}$ represent the maximum charge level for the battery and ultra-capacitor, respectively, as a proportion of their total capacity.

Consider the following definitions:

$$H = \theta_y^T W_y \theta_y + W_u \quad and$$
$$f = -2\theta_y^T W_y \left(y_{ref} - G_y x - Kr \right)$$

The calculation of the optimal control input at each step is performed by:

$$U_{opt}(k) = \min_{U} J = U^T H U + f^T U \qquad \text{4-11}$$

subject to

$$\Omega U \leq \omega \qquad \text{4-12}$$

The control algorithm is grounded on a receding horizon program, which involves applying the first control command, $u_{opt}(k)$, and then repeating the process.

4.3 Main considerations

The purpose of this chapter was to present concepts related to Model Predictive Control. The chapter outlined the mathematical modeling of this controller as an integral part of the overall microgrid modeling process.

5 System structure

5.1 Microgrid control loop

Once the EGS and the ESS are presented, the microgrid is displayed.

FIGURE 9 - MICROGRID SKETCH
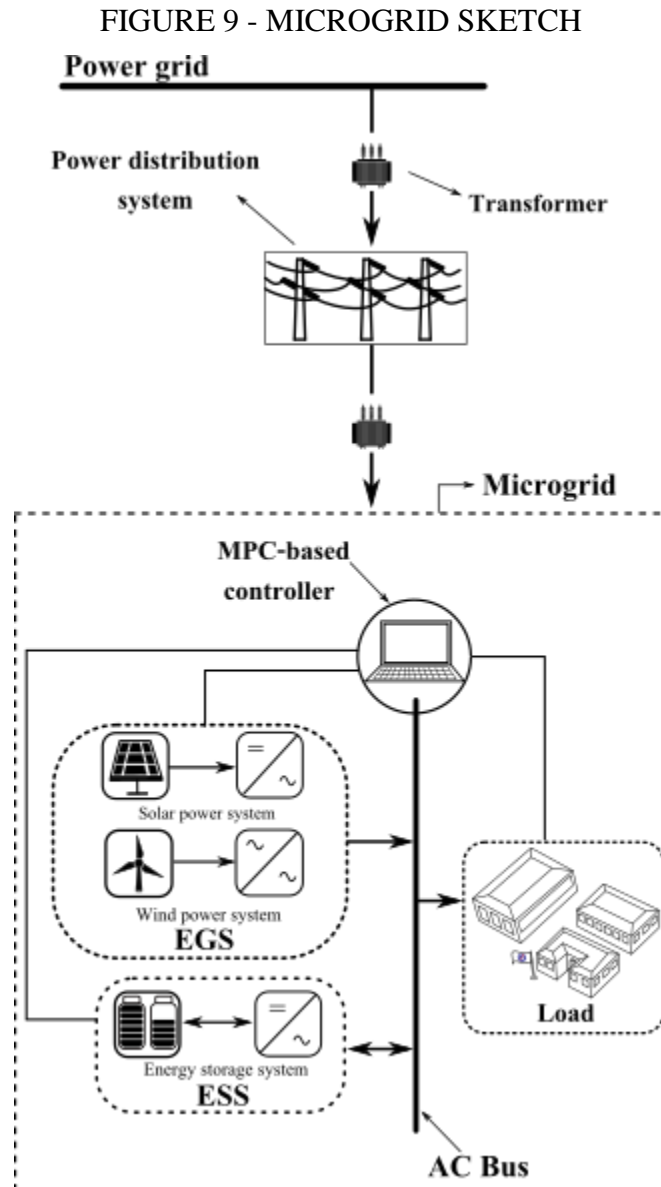
Observe from FIGURE 9 **Erro! Fonte de referência não encontrada.**that the microgrid comprises the energy generation system and the energy storage system, which were previously described. The EGS is made up of PV panels and a wind turbine that supply power to the microgrid, with power flowing in a unidirectional manner. The ESS comprises an assembly of energy storage mechanisms, comprising a battery and an ultra-capacitor, which can

both receive and discharge power to the grid depending on the charging or discharging needs of the system.

The preceding sections depict the MG's modeling, but they are deficient in expounding on the comprehensive operational aspects of the system.

The MPC, through the reference signal generator, receives information from the MG and impels its inputs to facilitate the power grid's synchronization with this signal. The reference signal generator periodically updates the signal every hour and as soon as it is stimulated, the algorithm suggested by the work is implemented.

FIGURE 10 **Erro! Fonte de referência não encontrada.**outlines the MG control loop's schematic representation.

FIGURE 10 - MICROGRID CONTROL LOOP
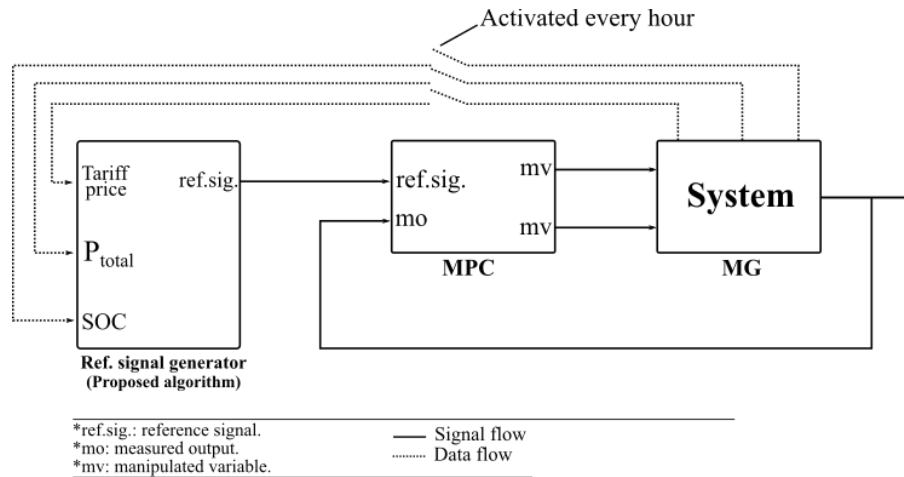
The diagram depicts the reference signal generator acquiring data from the MG system at regular intervals, with the switches indicating that the system activates every hour. When the set-point generator is triggered, the reference signal is updated and then transmitted to the controller. Note that the *system* block represents the microgrid.

5.2 The proposed model

The model under consideration presents both a deterministic and a stochastic variant. A deterministic procedure involves procedures unaffected by random phenomena, while a stochastic procedure inherently integrates unpredictable elements into its essence.

The present study introduces a theoretical framework, illustrated in FIGURE 10 by the reference signal generator block that comprises a cost function containing weighting parameters. The optimization process underlying the proposed model relies on this cost function, as

depicted in eq. $L = \min_{y_{ref}} \left(y_{ref} - \kappa \right)^2$ 5-1. The function aims to minimize the discrepancy between the reference signal and a constant that varies with the tariff price, the SOC of the ESS, and the grid power.

$$L = \min_{y_{ref}} \left(y_{ref} - \kappa \right)^2 \qquad\qquad 5\text{-}1$$

where

$$\kappa = \frac{1}{\lvert p_{tariff}(t) \rvert} \left(\delta P_{grid} + \alpha\, SOC_{bat}\, \mathrm{Pr}_{bat} + \beta\, SOC_{UC}\, \mathrm{Pr}_{UC} \right), \qquad 5\text{-}2$$

$\lvert p_{tariff}(t) \rvert$ is the magnitude of the energy tariff price at time t. δ, α, and β are the weighting parameters of the grid power, of the battery SOC, and of the UC SOC, respectively. Pr_{bat} and

$$\mathrm{Pr}_{bat} = Eq_{rbat}$$

Pr_{UC} are the battery and the UC average power, respectively, found through eq. $\mathrm{Pr}_{UC} = Eq_{rUC}$

5-3. Note that the terms that follow α and β are the average power that remains in the battery and in the UC, respectively, when the algorithm is performed.

$$\begin{aligned} \mathrm{Pr}_{bat} &= Eq_{rbat} \\ \mathrm{Pr}_{UC} &= Eq_{rUC} \end{aligned} \qquad\qquad 5\text{-}3$$

5.2.1 Deterministic variant of the model

The deterministic model operates on the premise that the user establishes and maintains constant weighted parameters for eq. $L = \min_{y_{ref}} \left(y_{ref} - \kappa \right)^2$ 5-1. The values assigned to these parameters remain unaltered unless modified by the user; in other words, the values of α, β, and δ do not change automatically based on system requirements. Consequently, the key task involves selecting values for these parameters that yield optimal technical-economic benefits for the microgrid under study. An empirical examination of the value ranges of the weighted parameters is necessary to identify values that provide the maximum advantages to the system.

By varying the parameters α, β, and δ, different weights are assigned to the variables under analysis, thereby altering the reference signal. Given the constancy of these values, loads with profiles exhibiting minimal changes over the course of days are expected to experience greater benefits.

5.2.2 Stochastic variant of the model

The stochastic version is crafted for online simulation. It has the capability to read the MG variables and search for the optimal set of three weighted parameter values during each iteration of the model.

For a thorough comprehension of the suggested model, refer to FIGURE 11. This diagram portrays a flowchart illustrating the functioning of the microgrid, the proposed model, and their interactions. The flowchart comprises a main flow that incorporates the microgrid and control systems, accompanied by a subsidiary branch outlining the routine of the stochastic variant of the proposed model.

FIGURE 11 - STOCHASTIC VARIANT OF THE MODEL FLOWCHART
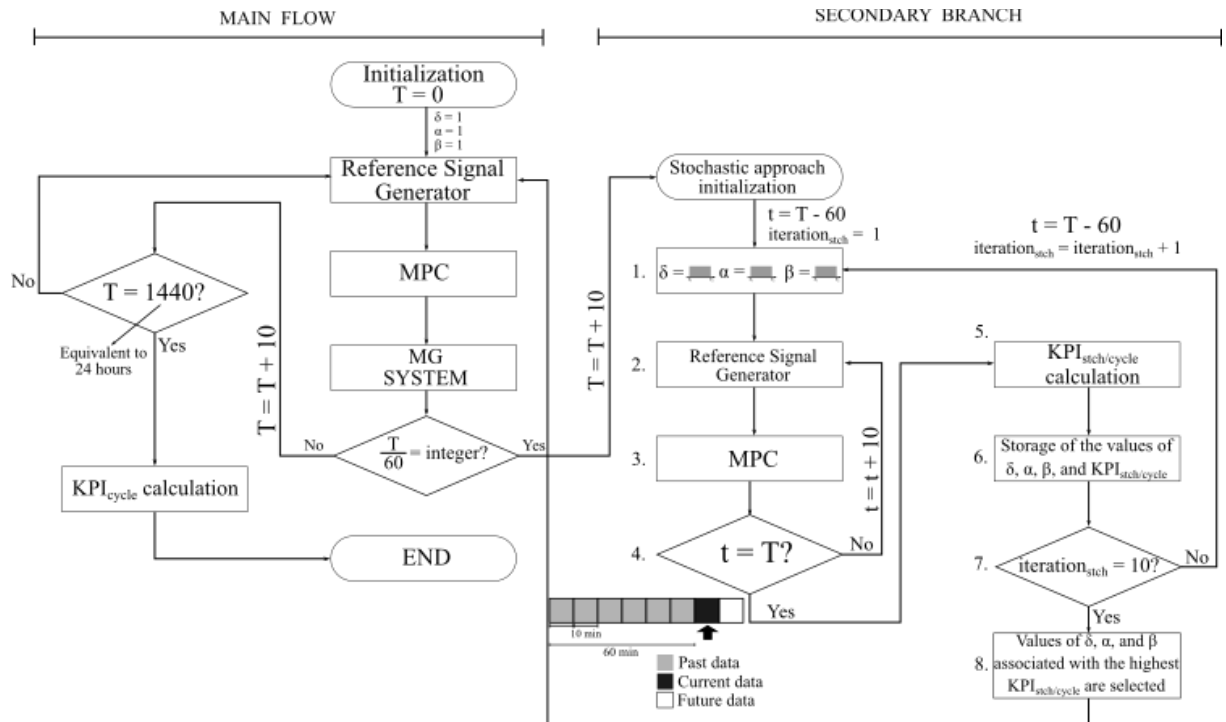
The algorithm commences by selecting the first data element with $T = 0$ and δ, α, and β set to 1.

The main branch of the flowchart is executed until the number of iterations equals an hour ($T = 60$). At each iteration, T increases by 10 minutes, and the management process of the microgrid and the generation of reference signals are conducted. In other words, the optimization system of the reference signal generator, as well as the MPC and the entire microgrid, are updated whenever the primary algorithm is executed. However, the values of δ,

α, and β remain constant until the secondary branch of the flowchart is executed, at which point the stochastic simulation is carried out to update these parameters.

As the stochastic approach employs variables whose values change randomly at each iteration, these variables must be linked to probability distribution functions based on the system's requirements to which the model will be applied. In this study, the parameters δ, α, and

$$f(z) = \begin{cases} \dfrac{1}{z_2 - z_1}, & for \quad z_1 \leq z \leq z_2 \\ 0, & otherwise. \end{cases} \qquad 5\text{-}4$$

β are linked to uniform distribution functions. Eq. displays the equation of this curve across the indicated range.

$$f(z) = \begin{cases} \dfrac{1}{z_2 - z_1}, & for \quad z_1 \leq z \leq z_2 \\ 0, & otherwise. \end{cases} \qquad 5\text{-}4$$

When T becomes a multiple of 60, the stochastic algorithm is activated, and the secondary branch of the flowchart executes a set of steps that repeat until $iteration_{stch} = 10$. The $iteration_{stch}$ variable signifies the count of iterations performed by the stochastic algorithm, with the initial value set to 1 and incremented by one unit after each interaction.

In the diagram secondary branch, previous data from the preceding hour is utilized to determine the optimal values of δ, α, and β and generate the reference signal for the following hour. The initial element that corresponds to the first 10 minutes of an hour is chosen ($t = T - 60$), and then the subsequent steps are executed. Upon completion of the steps sequence, the second element ($t + 10$) is selected, and so on. The algorithm continues until the final element of the series ($t = T - 10$) is attained, concluding the entire dataset.

The proposed algorithm follows a set of steps in the secondary branch of FIGURE 11, which is outlined below:

1. New values for δ, α, and β in eq.

$$\kappa = \frac{1}{|p_{tariff}(t)|}\left(\delta P_{grid} + \alpha SOC_{bat}\,Pr_{bat} + \beta SOC_{UC}\,Pr_{UC}\right), \qquad 5\text{-}2$$ are randomly assigned using a uniform distribution.

2. Eq. $$L = \min_{y_{ref}}\left(y_{ref} - \kappa\right)^2 \qquad 5\text{-}1$$ is carried out.

3. MPC is initiated to manage the grid power of the MG system.

4. The next observation in the row of past data is used. Steps 2, 3, and 4 are repeated until the final element of the row is reached.

5. The $KPI_{stch/cycle}$ is computed by analyzing all the elements of the dataset to estimate the cost of the system over the past hour.

6. The values of δ, α, β, and $KPI_{stch/cycle}$ are stored.

7. The preceding steps are repeated, and the values of δ, α, and β that are linked to the highest $KPI_{stch/cycle}$ value are chosen.

8. The newly determined values of δ, α, and β from step 7 are employed to produce the reference signal for the subsequent hour.

The KPI_{stch} is a metric that assesses the economic viability of the microgrid system with and without the energy storage system when the stochastic algorithm routine is executed. It is calculated by comparing the energy costs of the MG system with and without the ESS. The former is represented by the costs of the grid power, whereas the latter is represented by the costs of the total power. KPI_{stch} measures the cost-effectiveness of the MG system equipped with ESS and managed by the proposed model, as compared to the MG system without ESS.

Eqs. $Cost_{P_{grid}}{}^{stch} = p_{tariff}{}^{stch} \int_{T-60}^{T} P_{grid}(t)\,dt$ 5-5   and $Cost_{P_{total}}{}^{stch} = p_{tariff}{}^{stch} \int_{T-60}^{T} P_{total}(t)\,dt$

5-6 outline the calculation of costs utilized for estimating KPI_{stch}, which is derived through eq. $KPI_{stch} = Cost_{P_{grid}}{}^{stch} - Cost_{P_{total}}{}^{stch}$ 5-7.

$$Cost_{P_{grid}}{}^{stch} = p_{tariff}{}^{stch} \int_{T-60}^{T} P_{grid}(t)\,dt \qquad\qquad 5\text{-}5$$

$$Cost_{P_{total}}{}^{stch} = p_{tariff}{}^{stch} \int_{T-60}^{T} P_{total}(t)\,dt \qquad\qquad 5\text{-}6$$

$$KPI_{stch} = Cost_{P_{grid}}{}^{stch} - Cost_{P_{total}}{}^{stch} \qquad\qquad 5\text{-}7$$

The variables P_{grid} and P_{total} results in the corresponding grid energy and total energy values for the specified integration interval. An essential technical aspect in microgrid operations pertains to the quantity of duty cycles for the ESS. The system is engineered with a specified constraint on duty cycles, a factor that directly impacts its operational lifespan. As the ESS undergoes more cycles, its anticipated lifespan diminishes. To optimize the longevity of the ESS, it is advisable to restrict the number of cycles it undergoes.

To tackle constraints on the algorithm arising from both economic and technical considerations, symbolized by KPI_{stch} and the number of duty cycles of the ESS — a refined formulation of the KPI has been introduced, incorporating both these dimensions.

$$KPI_{stch/cycle} = \frac{KPI_{stch}}{Total\ duty\ cycles\ of\ ESS\ in\ a\ given\ iteration} \qquad 5\text{-}8$$

where the denominator indicates the cumulative number of duty cycles for both energy storage devices in a specific iteration.

The calculation of duty cycles for the ESS occurs whenever the SOC of any of the ESS devices reaches or drops below 20% of the device's total SOC, rises to or exceeds 80% of that device's SOC level, and subsequently returns to a level at or below 20%. When the SOC follows this pattern, it results in the counting of one cycle.

The distinction between KPI_{stch} and $KPI_{stch/cycle}$ lies in their areas of assessment: the former exclusively measures the economic value of the microgrid, while the latter quantifies both economic and technical dimensions. It is important to note that the calculation of $KPI_{stch/cycle}$ is directly linked to the value of KPI_{stch} and inversely proportional to the number of duty cycles of the ESS. This indicates that the $KPI_{stch/cycle}$ value is likely to increase as the financial return through KPI_{stch} rises and as the number of ESS duty cycles decreases. In summary, higher values of $KPI_{stch/cycle}$ indicate robust financial returns, minimal utilization of the storage system, or a combination of both factors. Thus, achieving elevated values for this metric is desirable.

5.3 Main contributions

The purpose of this chapter is to depict the proposed microgrid structure. However, its main assignment is to present the work's suggested algorithm for generating the reference signal.

6 Case Study

In order to authenticate the proposed research model, a case study is formulated and assessed. The equipment information pertaining to MG is sourced from the manufacturers' data sheets, readily accessible on their official websites. Conversely, data related to wind, solar irradiance, and load is procured from the university laboratories and collected throughout the year 2017.

The present regulations of the Brazilian energy sector do not encompass time-of-use energy tariffs, i.e., tariffs with fluctuating prices at different times of the day. Nonetheless, in anticipation of prospective market transformations, the case study scenarios take into consideration hourly prices of the energy tariff to scrutinize the results of the proposed model when the regulations alter.

6.1 Used data

The load simulation data originates from the facilities of the Federal University of Itajubá. The data were utilized in its original form as well as in an altered state. When referring to the term *original*, it is understood that the description pertains to information obtained and remaining unaltered, thus preserving its raw condition. The altered data have been subject to modifications specifically for the objectives of this research.

The data obtained are not sufficiently diverse, necessitating modifications to the original dataset. These adjustments aim to determine if the variations introduced in the proposed model enhance the microgrid's resilience against significant alterations in the load profile. These alterations are carried out in a manner that modifies the daily data average.

Note, in FIGURE 12 the original and the modified data.

FIGURE 12 - ORIGINAL AND MODIFIED DATA ACQUIRED
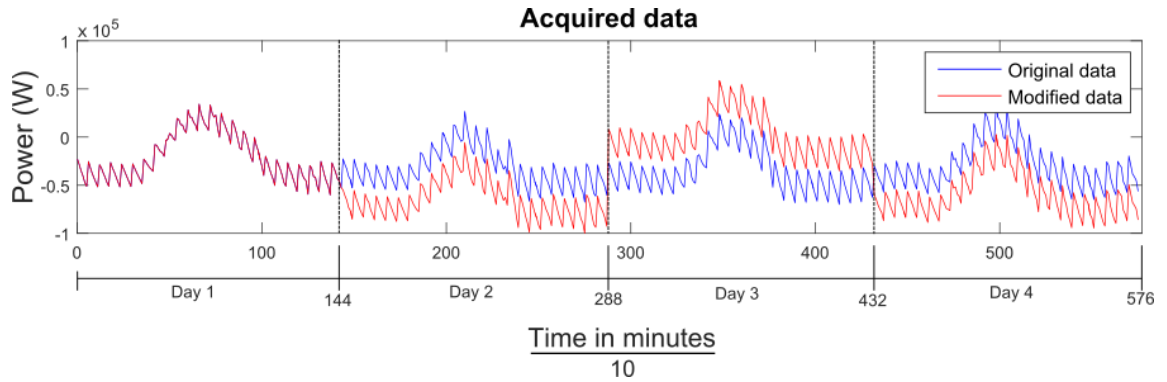
The data depicted in the image represent P_{total}, calculated at 10-minute intervals. Each window of the graph corresponds to a full day. The blue curve signifies the original data, while the red curve illustrates the modified data based on the following criteria:

- For day 1: The modified data matches the original data of day 1.
- For day 2: The modified data is calculated as the original data of day 2 plus μ_2.
- For day 3: The modified data is derived from the original data of day 3 minus μ_3.
- For Day 4: The modified data is the sum of the original data of day 4 and μ_4.

where μ_2, μ_3, and μ_4 represent the averages of the original data for days 2, 3, and 4, respectively.

6.2 Specifications of the microgrid components

The study drew upon the parameter specifications of the Hummer H17 0-50kW turbine, a product of the Chinese manufacturer Anhui Hummer Dynamo Company Ltd. (WIND TURBINE MODELS, 2022). Additionally, the parameters for the PV panels were sourced from the Canadian Solar BiHiKu 390-415 W module, a PV panel designed by Canadian Solar (CANADIAN SOLAR, 2023).

Pertaining to the ESS, the parameters have been sourced from the official datasheets provided by battery and ultracapacitor manufacturers (ELETRICIDADE MODERNA, 2023; SKELETON+, [s.d.]).

Erro! Fonte de referência não encontrada. presents the parameters and their respective values for each system comprising the MG.

TABLE 2 - THE PARAMETERS' VALUES OF THE SYSTEMS.

Variable symbol	Variable description	Value
Wind power system		

d	Rotor diameter	17
ρ	Air density	1.225
C_p	Wind turbine power coefficient	$C_p = -6.052\times10^{-4}v^6 + 2.182\times10^{-2}v^5 - 0.3129v^4 + 2.264$ 2-6 $R^2 = 1 - \dfrac{\sum(y_i - \hat{y}_i)^2}{\sum(y_i - \overline{y})^2}$ 2-5 $C_p(v) = a_{(n)}v^n + a_{(n-1)}v^{n-1} + ... + a_0$ 2-4
v	Wind speed	Dataset
P_r	Turbine rated power	50k

PV power system		
P_{stc}	Power under STC	400
NOCT	Nominal Operation Cell Temperature	41
G_{NOCT}	Irradiance under NOCT	800
G	Irradiance over the module	Dataset
γ	Coefficient of maximum power	0.0036
T_{cell}	Cell temperature	$T_{cell} = T_{amb} + \dfrac{G}{G_{NOCT}}\left(NOCT - T_{amb,NOCT}\right)$ 2-9
N_{pv}	Number of photovoltaic modules	100

Battery system		
Rs_{bat}	Internal series resistance	0.001
Rp_{bat}	Internal parallel resistance	0.001
C_{bat}	Internal capacitance	1.00E+06
q_{rbat}	Charge capacity	2000
$soc_{max(bat)}$	Maximum SOC	0.9
$soc_{min(bat)}$	Minimum SOC	0.1
i_{bat}	Current operating range	[-3000,3000]

UC system		
Rs_{UC}	Internal series resistance	2.40E-04
Rp_{UC}	Internal parallel resistance	1000
C_{UC}	Capacitance	63
q_{rUC}	Charge capacity	200
$soc_{max(UC)}$	Maximum SOC	0.9
$soc_{min(UC)}$	Minimum SOC	0.1
i_{UC}	Current operating range	[-1000,1000]

6.3 Proposed scenarios

The dataset consists of observations taken every 10 minutes, with a time interval of $\Delta t = 1/6$ hours, over the course of a year. However, due to the high data processing requirements resulting from the large number of samples, and the fact that the study does not require access to the entire database, the model analysis considered only the data collected over a 24-hour period.

Two scenarios are considered in this work and they are described as follows.

- **Scenario 1:** In this scenario, the electricity tariff has two distinct rates:
  - During off-peak hours, when the national power grid experiences lower demand, the tariff is priced at 0.20 US$/kWh.
  - During peak hours, the tariff increases due to higher demand and is priced at 1.00 US$/kWh, which is five times the off-peak rate.

In Brazil, peak hours are defined as the period between 6 p.m. and 9 p.m.

- **Scenario 2:** In this scenario, the energy tariff follows a continuous and incremental pattern, without distinct peak or off-peak periods. The tariff begins at a nominal rate of 0.10 US$/kWh at 12 a.m. and increases by 10 cents every hour. By the end of the 24-hour cycle, just before 12 a.m. the next day, the cost culminates at 2.40 US$/kWh.

Both the scenarios are similar, with the only difference being the tariff policy implemented by the local energy market. As a result, the equations used to calculate the KPI vary depending on the scenario being analyzed.

In scenario 1, the equations used to calculate the KPI are eqs.

$$Cost_{P_{grid}}{}^{sc1} = p_{off\_peak}\left(\int_{12a.m.}^{6p.m.} P_{grid,res.}(t)\,dt + \int_{9p.m.}^{12a.m.} P_{grid,res.}(t)\,dt \right) + p_{peak} \int_{6p.m.}^{9p.m.} P_{grid,res.}(t)\,dt$$

6-1,

$$Cost_{P_{total}}{}^{sc1} = p_{off\_peak}\left(\int_{12a.m.}^{6p.m.} P_{total,res.}(t)\,dt + \int_{9p.m.}^{12a.m.} P_{total,res.}(t)\,dt \right) + p_{peak} \int_{6p.m.}^{9p.m.} P_{total,res.}(t)\,dt$$

6-2, and

$$KPI^{sc1} = Cost_{P_{grid}}{}^{sc1} - Cost_{P_{total}}{}^{sc1}$$

6-3. In scenario 2, the KPI is calculated using eq.

$$Cost_{P_{grid}}{}^{sc2} = \sum_{t=1}^{24}\left(p_{tariff}(t) \int_{t-1}^{t} P_{grid,res.}(t) \right) \qquad Cost_{P_{total}}{}^{sc2} = \sum_{t=1}^{24}\left(p_{tariff}(t) \int_{t-1}^{t} P_{total,res.}(t) \right)$$

6-4, 6-5,

and $KPI^{sc2} = Cost_{P_{grid}}{}^{sc2} - Cost_{P_{total}}{}^{sc2}$

6-6. The choice of which set of equations to use de-

pends on the specific scenario being analyzed, as the energy market rules and tariff policies differ between the two scenarios.

$$Cost_{P_{grid}}{}^{sc1} = p_{off\_peak}\left(\int_{12a.m.}^{6p.m.} P_{grid,res.}(t)\,dt + \int_{9p.m.}^{12a.m.} P_{grid,res.}(t)\,dt\right) + p_{peak}\int_{6p.m.}^{9p.m.} P_{grid,res.}(t)\,dt \qquad 6\text{-}1$$

$$Cost_{P_{total}}{}^{sc1} = p_{off\_peak}\left(\int_{12a.m.}^{6p.m.} P_{total,res.}(t)\,dt + \int_{9p.m.}^{12a.m.} P_{total,res.}(t)\,dt\right) + p_{peak}\int_{6p.m.}^{9p.m.} P_{total,res.}(t)\,dt \qquad 6\text{-}2$$

$$KPI^{sc1} = Cost_{P_{grid}}{}^{sc1} - Cost_{P_{total}}{}^{sc1} \qquad 6\text{-}3$$

$$Cost_{P_{grid}}{}^{sc2} = \sum_{t=1}^{24}\left(p_{tariff}(t)\int_{t-1}^{t} P_{grid,res.}(t)\right) \qquad 6\text{-}4$$

$$Cost_{P_{total}}{}^{sc2} = \sum_{t=1}^{24}\left(p_{tariff}(t)\int_{t-1}^{t} P_{total,res.}(t)\right) \qquad 6\text{-}5$$

$$KPI^{sc2} = Cost_{P_{grid}}{}^{sc2} - Cost_{P_{total}}{}^{sc2} \qquad 6\text{-}6$$

KPI^{sc1} and KPI^{sc2}, calculated using eqs. $KPI^{sc1} = Cost_{P_{grid}}{}^{sc1} - Cost_{P_{total}}{}^{sc1}$ 6-3   and

$KPI^{sc2} = Cost_{P_{grid}}{}^{sc2} - Cost_{P_{total}}{}^{sc2}$ 6-6 respectively, indicate the feasibility of the proposed MG in scenario 1 and 2 compared to an MG without the ESS. It is important to note that the calculation of costs for estimating these performance indices is done for a period of 24 hours and does not include investment or system maintenance costs. Therefore, the *KPI* is an index that only considers energy costs for a day and disregards other types of expenses. A positive *KPI* value indicates that the proposed management system makes the MG more economically profitable in comparison with an MG without this system. A negative *KPI* value, on the other hand, indicates that the proposed system is not financially feasible.

FIGURE 13 depicts a schematic representation that encapsulates the assemblage and utilization of the datasets employed for the authentication of the suggested model. Additionally, the aforementioned figure showcases the tariff price policy implemented in each of the investigated scenarios.

FIGURE 13 - (a) DATASETS UTILIZED IN THE RESEARCH, AND (b) ENERGY TARIFF PRICING POLICIES IN EACH RESPECTIVE SCENARIO
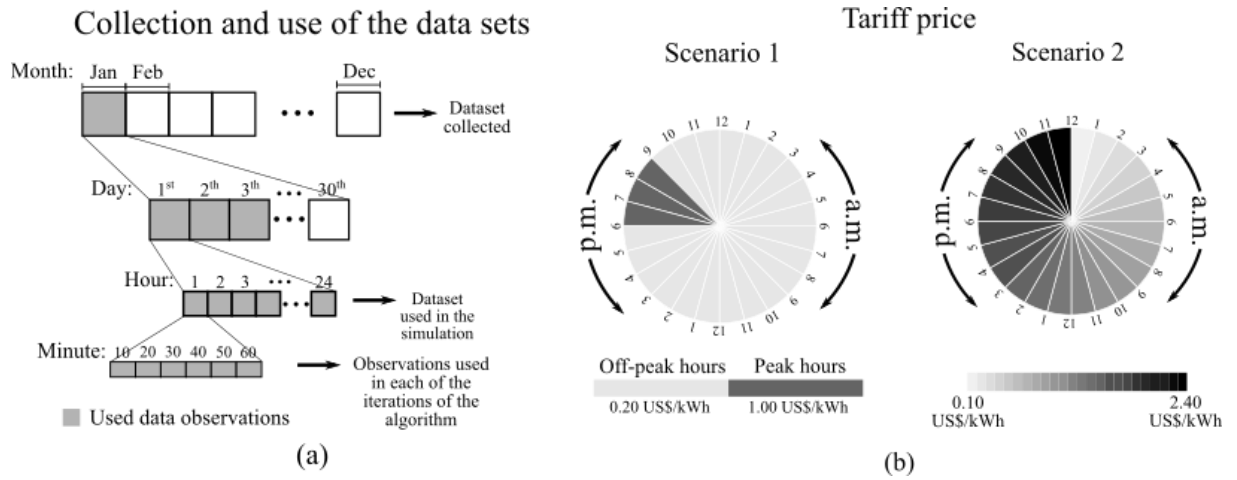
7 Benchmark models

To test the effectiveness of the proposed model, a comparison with well-established benchmark models in the literature was conducted. One of the models used as a reference is Fuzzy Logic, based on rules, and it was chosen considering its high applicability in other works similar to the current study (ANGALAESWARI et al., 2017; BHATTACHARYA; CHATTERJEE; GOSWAMI, 2023; HARTANI et al., 2022; MEHTA; BASAK, 2023; RODRIGUEZ; ARCOS-AVILES; GUINJOAN, 2024).

Another employed model is the Whale Optimization Algorithm (WOA), based on optimization techniques. Its selection stems from its relative novelty, having been introduced to the scientific community in 2016 (MIRJALILI; LEWIS, 2016).

The aim of this current study is to introduce, simulate, and evaluate a new microgrid management model within specific characteristics. However, the comparison with other methods underscores the significance of this model for advancing the field of electrical network control.

The proposed model, as well as the benchmarks, have parameters and variables that, when altered, change their results. Consequently, a variety of model configurations can be established, resulting in different outputs. After testing various configurations, those that yielded the best results were selected and are presented in this document.

7.1 Fuzzy Logic benchmark analysis

Fuzzy Logic constitutes a division of mathematical logic concerned with the concept of partial truth, in contrast to classical logic, which exclusively accommodates absolute truth values (true or false). Its primary application lies in the modeling of intricate systems wherein responses exhibit a continuum and extend beyond discrete binary outcomes.

The general flow of fuzzy processing is: to take precise inputs, fuzzify them, apply fuzzy rules to achieve a fuzzy output, and subsequently defuzzify this output to obtain a clear, precise value.

Fuzzification is understood as the process by which a crisp input value is converted into a fuzzy value, translating precise values into degrees of membership within a fuzzy set. Fuzzy rules, established using natural language, dictate the application of this logic and are transformed for computational purposes. After such application, a clear or crisp response is typically sought. This return to clarity is termed defuzzification, where a fuzzy value is reverted to

a precise value. Several techniques facilitate this process, including the centroid method and the weighted bisector, among others.

In the proposed study, the input variables are: P_{total}, SOC_{bat}, SOC_{UC}, and *Tariff Price*, whereas the output variable is P_{grid}. These variables are subjected to Fuzzy member functions as illustrated in FIGURE 14, the defuzzification procedures are executed employing the centroid method.

Note that the configuration of the membership functions can be established in a multitude of ways, and each configuration leads to different outcomes. This implies that there may be sets of membership functions that yield better results than others; however, the chosen configuration is sufficient for the comparison of the proposed model.

Over a thousand rules have been applied to the implementation of the technique, but they have been excluded from this document for the sake of readability.

FIGURE 14 - FUZZY MEMBER FUNCTIONS
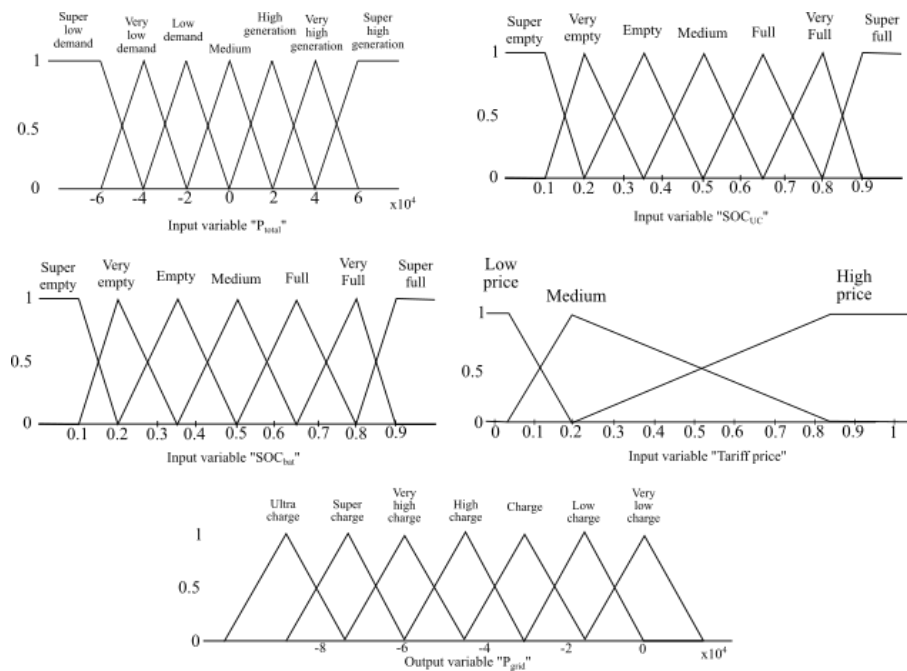
7.2 Whale Optimization Algorithm

The Whale Optimization Algorithm (WOA) is a computational technique inspired by the hunting behavior of humpback whales. The WOA was selected as a benchmark in this study for two primary reasons: it represents a contemporary approach, published in 2016, and shares the foundation of optimization with the algorithm proposed in this work.

The WOA mimics the movement patterns of these whales as they search for prey, utilizing a spiral motion to imitate the bubble-net hunting strategy characteristic of humpback whales.

It is a well-established fact that whales exhibit both solitary and group behaviors, with the latter being more commonly observed. Certain whale species, such as killer whales, are known to form familial groups that persist throughout their entire lifespans. Among the largest baleen whales is the humpback whale (Megaptera *novaeangliae*), which can reach sizes comparable to that of a school bus. Humpback whales primarily feed on krill and small schools of fish. FIGURE 15 provides a visual representation of this marine mammal.

FIGURE 15 - BUBBLE-NET FEEDING BEHAVIOR OF HUMPBACK WHALES
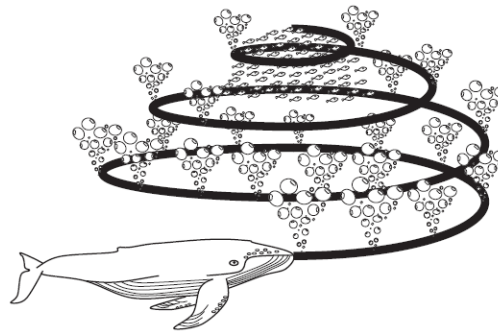
SOURCE: MIRJALILI; LEWIS (2016).

The WOA, pioneered by Mirjalili and Lewis in their 2016 paper (MIRJALILI; LEWIS, 2016), has been chosen for integration into the present investigation owing to its recent inception.

According to the authors' claim, considering the uncertain whereabouts of the optimal design within the exploration zone, the WOA theory posits that the current leading candidate solution either embodies the desired prey or lies close to the optimum. After pinpointing the top-performing search agent, the rest of the search agents strive to realign their positions in accordance with the best search agent.

The procedure comprises three clear stages: the encirclement phase, the bubble-net attack strategy, and the prey search phase. In the encirclement phase, humpback whales locate the prey and proceed to surround it. Considering the uncertain position of the optimal design within the search space, the WOA suggests that the current top candidate solution either embodies the target prey or is near the optimal solution. Subsequent to identifying the best search agent, the rest of the search agents strive to align their positions with this optimal agent.

In the bubble-net predatory technique, humpback whales navigate around the prey within a diminishing loop and along a coil-shaped trajectory at the same time. To emulate this concurrent conduct, it is posited that there exists an equal likelihood of 50% to opt for either the diminishing encircling mechanism or the spiral blueprint for adjusting the whales' position during optimization.

Throughout the prey-hunting phase, humpback whales partake in stochastic exploration guided by the locations of their companions. The search agents are stimulated to venture considerably away from a designated whale and modify their positions according to a randomly chosen search agent, instead of solely following the presently recognized optimal search agent. This mechanism highlights the significance of exploration, allowing the WOA to execute an exhaustive global search.

Humpback whales exhibit the ability to locate and encircle prey. Given that the precise location of the optimal design within the search space is not initially known, the WOA operates under the assumption that the current best candidate solution represents the target prey or is in close proximity to the optimum. Once the best search agent is identified, the remaining search agents endeavor to adjust their positions towards this optimal search agent. This behavioral pattern is expressed through the following equations:

$$\vec{D} = |\vec{C}\vec{X}^{*}(t) - \vec{X}(t)|$$
$$\vec{X}(t+1) = \vec{X}^{*}(t) - \vec{A} \cdot \vec{D}$$

7-1

In the context of the current iteration, the symbols A e C represent coefficient vectors, while X^* denotes the position vector corresponding to the best solution achieved thus far. Moreover, X represents another position vector, $|\ |$ signifies the absolute value, and $\cdot$ denotes element-wise multiplication. It is important to note that X^* should be consistently updated during each iteration if a superior solution is found.

The computation of vectors A and C is carried out in the following manner:

$$\vec{A} = 2\vec{a} \cdot \vec{r} - \vec{a}$$
$$\vec{C} = 2 \cdot \vec{r}$$

7-2

where the parameter a undergoes linear reduction from 2 to 0 throughout iterations, encompassing both exploration and exploitation phases, while r represents a random vector within the range of [0,1].

The update of a search agent's position (X, Y) can be determined relative to the position of the current best record (X^*, Y^*). By adjusting the values of vectors A and C, various positions around the best agent can be attained in relation to the current position. Thus, the algo-

rithm facilitates the adjustment of any search agent's position within the vicinity of the current best solution, effectively simulating the process of encircling the prey.

The updating of the vector position follows a spiral-based methodology, initiating with the computation of the distance between the whale positioned at (X, Y) and the prey located at (X^*, Y^*). Subsequently, a spiral equation is formulated between the whale's position and that of the prey, emulating the helical movement characteristic of humpback whales. This equation is expressed as follows:

$$\vec{X}(t+1) = \vec{D'} \cdot e^{bl} \cdot \cos(2\pi l) + \vec{X^*}(t) \qquad\qquad 7\text{-}3$$

where the vector D represents the distance denoted by the ith whale to the prey, calculated as $|X^*(t) - X(t)|$. $X^*(t)$ and $X(t)$ correspond to the current positions of the prey (best solution obtained so far) and the ith whale respectively. The constant b is utilized to determine the shape of the logarithmic spiral, while l stands for a randomly generated number within the interval [-1,1]. Additionally, the symbol '.' signifies element-wise multiplication.

It is pertinent to note that humpback whales engage in simultaneous maneuvers, encircling prey within a shrinking circle and traversing along a spiral-shaped trajectory. In order to emulate this concurrent behavior, we introduce a probabilistic framework wherein there exists a 50% probability of selecting either the shrinking encircling mechanism or the spiral model to update the positions of the whales during the optimization procedure. The mathematical formalization of this model is articulated as follows:

$$\vec{X}(t+1) = \begin{cases} \vec{X^*}(t) - \vec{A} \cdot \vec{D} & if \ p < 0.5 \\ \vec{D'} \cdot e^{bl} \cdot \cos(2\pi l) + \vec{X^*}(t) & if \ p \geq 0.5 \end{cases}$$

where p is a random number in [0,1].

For additional details regarding WOA and the mathematical formulation of the equations composing this optimization model, please consult (MIRJALILI; LEWIS, 2016). The parameter values utilized in the implementation within the present study are obtained from the case study conducted by Mirjalili and Lewis.

The WOA, implemented in MatLab, is available as open-source code on GitHub. This source code was adapted and subsequently employed for the specific purposes of this research.

8 Results and discussion

In this study, the findings are examined based on the given scenarios and dataset utilized.

8.1 Comparison of methods

Four strategies are utilized for microgrid management: the proposed method in both deterministic and stochastic forms, Fuzzy Logic, and WOA. These approaches were applied using both: unaltered and adjusted datasets, simulating diverse load profiles. Additionally, two time-of-use scenarios were explored: one involving moderate tariff adjustments and another with significant tariff fluctuations.

In the proposed deterministic model, the weighting parameters are constants, set by the user. Observe the map in FIGURE 16 which illustrates the results for KPI_{cycle} based on distinct values of β and δ (with $\alpha = 0.01$) applied across various load profiles and proposed scenarios.

FIGURE 16 - MAP OF THE RESULTS FOR KPI~stch/cycle~

KPI~stch/cycle~ (US$)

Set of maps with original data scenario 1

Set of maps with modified data scenario 1

Set of maps with original data scenario 2

Set of maps with modified data scenario 2
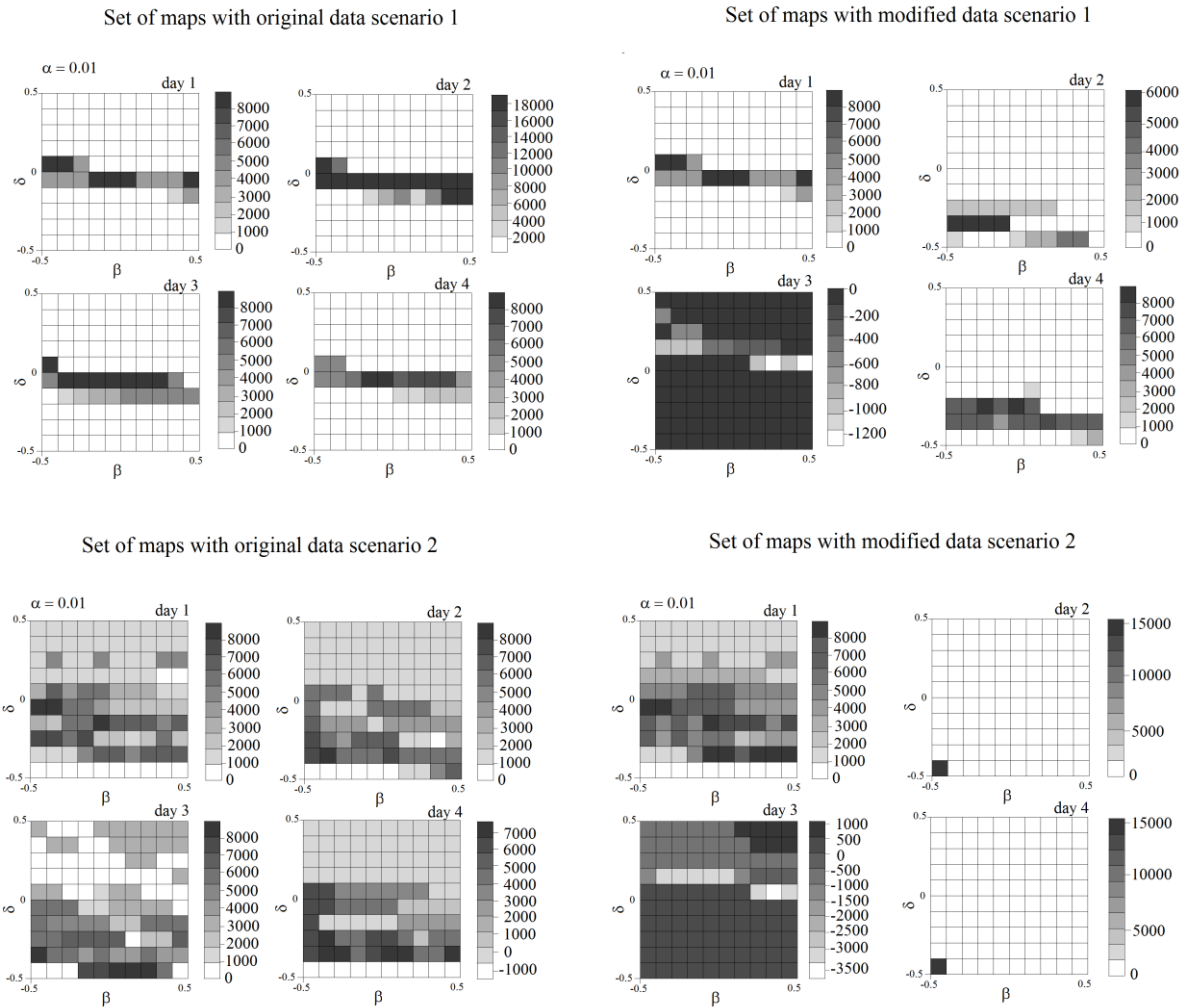
Upon analyzing the results from the simulation using the original data in scenario 1, a specific range of values for β and δ is identified wherein the *KPI~cycle~* exhibits high values across the four evaluated days. To clarify further, in cases where load profiles experience minimal fluctuations, both in load demand and energy tariff prices over the course of the day, significant financial and technical benefits can be attained for the microgrid by carefully selecting parameter values for the proposed model. Consider, for example, that the parameter set [α = 0.01, β = −0.1, δ = −0.1] yields optimal returns for the microgrid when utilizing raw data in scenario 1, regardless of the particular day under analysis.

Employing the original dataset in scenario 2, the map in FIGURE 16 indicates that parameter sets that result in high *KPI~cycle~* values are less frequent. In other words, the parameter combinations that generate optimal returns differ based on the analyzed day.

Regarding the simulations conducted with the modified data, for any proposed scenario, the deterministic model consistently displays high values of *KPI~cycle~* across all days. However,

70

the values of the weighted parameters leading to these high results differ for each day. The results obtained in this study are apt for offline analysis, yet they do not align optimally with the online configurations commonly adopted in commercial settings. It is essential to note that in the deterministic model, where the weighted parameters remain constant, the user — lacking foresight into the day's load profile — faces challenges in predicting the parameter values necessary to optimize KPI_{cycle}.

The stochastic version of the proposed model closely resembles the deterministic one. However, there is a distinction in that the values of the weighted parameters vary with each iteration of the algorithm. The parameter values linked to the highest Key Performance Indicator ($KPI_{stch/cycle}$) are chosen. The user defines the range within which the parameters can fall on a uniform distribution curve, and this directly influences the outcomes. This range is illustrated as z_1 and z_2 in eq. $f(z) = \begin{cases} \dfrac{1}{z_2 - z_1}, & for \quad z_1 \leq z \leq z_2 \\ 0, & otherwise. \end{cases}$ 5-4. For each stochastic variable, the specified limits are: $\alpha = [0.01; 0.1]$, $\beta = [-1; 1]$, and $\delta = [0.5; 2]$. While other value ranges were tested, the aforementioned range yielded the highest $KPI_{stch/cycle}$ return for the microgrid.

For every analyzed day, the stochastic version of the proposed model undergoes three simulations, and the average outcome is compared with the results obtained from other models.

Erro! Fonte de referência não encontrada.illustrates the outcomes of the KPI_{cycle} for the proposed model, Fuzzy Logic, and WOA, thus elucidating the advantages that each model offers to the microgrid.

FIGURE 17 - COMPARISON OF KPI_{cycle}
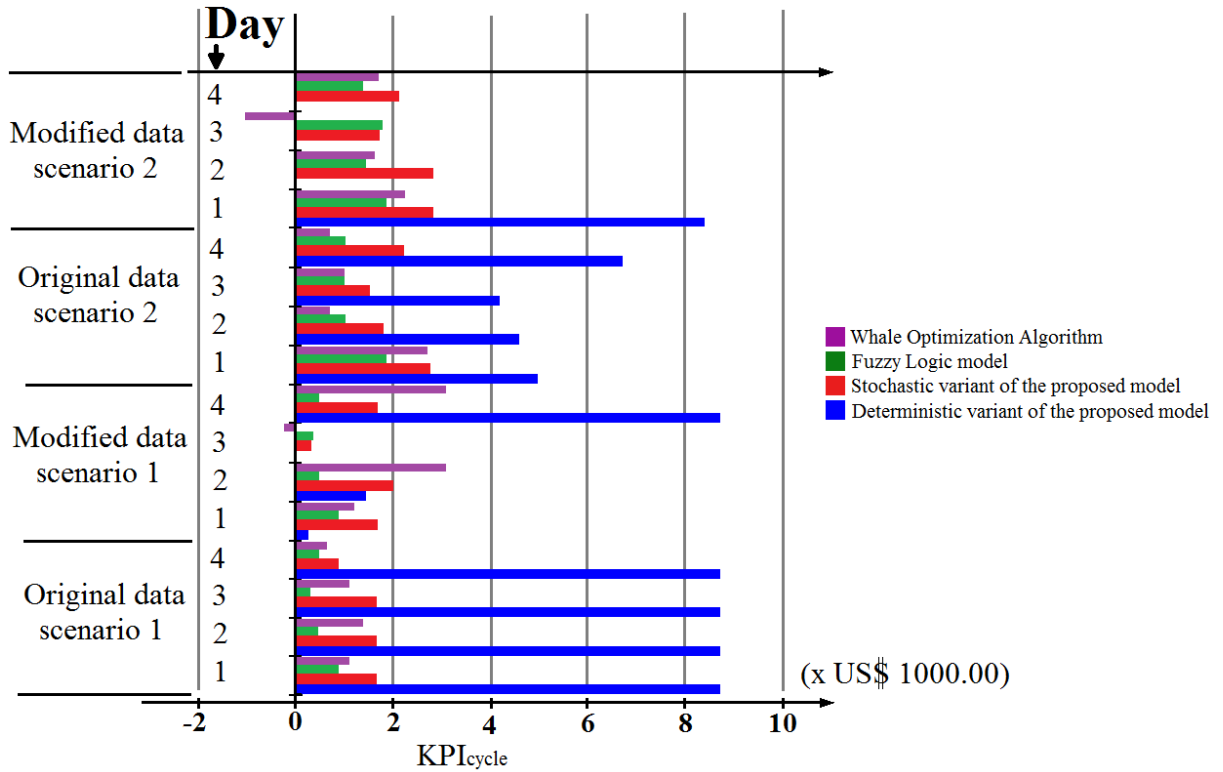
It is noteworthy that, in the deterministic variant of the proposed model, a distinct set of values for α, β, and δ was employed for each evaluated scenario to ensure a high KPI_{cycle}. In each scenario, four sets of values were utilized. For scenarios characterized by smoother load profiles, exemplified by the original load profile in scenario 1, the prescribed set of values for α, β, and δ is [0.01; -0.1; -0.1], respectively.

In scenario 2, the designated set of values is [0.01; -0.4; -0.3]. Conversely, for the adapted load profile in scenario 1, the assigned values are [0.01; -0.3; -0.3]. In scenario 2, these values are adjusted to [0.01; -0.1; -0.3].

The examination of FIGURE 17 reveals that the deterministic iteration of the proposed model provides noteworthy advantages to the microgrid, particularly in cases involving the utilization of the raw data. In scenarios employing the original data, the KPI_{cycle} is up to three times higher compared to the other models tested in scenario 2 and approximately six times higher in scenario 1. Nonetheless, it is imperative to note that this deterministic model does not confer significant benefits to the network in scenarios characterized by load profiles exhibiting abrupt variations along the days of the week.

Concerning the stochastic iteration of the model, it becomes apparent that the KPI_{cycle} values are notably lower than those of the deterministic model when using original data, but higher when modified data are utilized. Moreover, when compared to Fuzzy Logic, the sto-

chastic variant consistently presents significant advantages for the microgrid in all examined scenarios. Conversely, in contrast with the WOA, the model exhibits considerable benefits on most days.

The proposed model, whether in its deterministic or stochastic form, offers superior benefits to the microgrid compared to the assessed benchmark models. Quantitatively, the deterministic version yields substantial returns to the system for load profiles characterized by minimal fluctuations, commonly encountered in commercial settings. Conversely, the stochastic variant proves more advantageous for profiles exhibiting abrupt load variations.

Due to its inherent randomness, the stochastic model inherently presents a potential uncertainty for the microgrid; specifically, the algorithm's simulation yields varying values of KPI_{cycle} with each iteration. Although this uncertainty is not the primary focus of this study, its examination is crucial for the effective deployment of the proposed model within the microgrid. This analysis serves to alert the user to the potential for adverse outcomes.

Another crucial aspect to take into account concerns the constraint of the stochastic algorithm. When the algorithm's parameters are linked to a uniform distribution function, the range of this function's limits becomes paramount, directly influencing the outcomes of KPI_{cycle}. Hence, the meticulous selection of this range emerges as a pivotal determinant for the algorithm's effectiveness, necessitating the choice of a range conducive to yielding satisfactory results.

With that being said, it is recommended to carry out a comprehensive investigation of the deterministic version of the model prior to incorporating the stochastic variation. This examination aims to ascertain the weighted parameter values that significantly contribute to the microgrid's benefit. In essence, the deterministic variant of the model should be deployed and scrutinized initially, preceding the integration of the stochastic variant.

The findings of this study align with recent publications in the literature pertaining to new microgrid management models. The study of Abunima et al. (2022) introduces an innovative microgrid control approach that resulted in an approximate 20% cost reduction compared to the benchmark model. Similarly, the work of Fang et al. (2022) presents a microgrid management model that decreases the system's operational costs by 37%.

In line with the referenced studies, both iterations of the control model examined in this research provide advantages to the microgrid. Upon quantitative assessment of the models' outcomes using the KPI_{cycle} for each investigated scenario, it is evident that in the most favor-

able scenario, the deterministic variant demonstrates a KPI six times higher, while the stochastic variant, despite presenting a modest KPI_{cycle}, still surpasses the benchmark models.

8.2 Main considerations

The purpose of this chapter was to introduce the case study for validation of the proposed algorithm. Furthermore, the obtained results and some discussion were presented.

9 Conclusion

This study introduces a microgrid management model equipped with adjustable weighted parameters. This model provides two variants: deterministic and stochastic. The model and its variants aim to optimize both technical and economic aspects of the microgrid, taking into account diverse load profiles, tariff policies, and types of energy storage. To validate its effectiveness, the model's results are benchmarked against those of an approach well-established in the literature.

The findings indicated that, on the days examined, the deterministic variant of the proposed model yields a significant technical-financial return to the microgrid. The selection of the values for the weighted parameters directly influences this return. The deterministic variant is especially effective for more consistent load profiles, such as the original load used in the simulation. For loads with profiles that vary substantially over the days, this version of the model does not offer notable technical-financial benefits to the microgrid. In these cases, the stochastic variant displays more pronounced results compared to the deterministic variant, and more modest results when benchmarked against the reference model from the literature. However, in general, when the system displays sharp load fluctuations, the stochastic variant offers superior benefits to the microgrid compared to the other models.

Within the context of various tariff policies, the advantages of the proposed model were notably quantitative. However, the observed benefits are more closely tied to the characteristics of the analyzed scenarios than to the model itself. In summary, although the comparison between different tariff scenarios shows significant advantages of one over the other, these advantages are not as apparent when comparing the results among different microgrid management models.

It is essential to highlight that, during the development of this study, empirical tests were conducted with the weighted parameters of the proposed model and with the rules of Fuzzy Logic. These tests aimed to fine-tune both techniques to produce the best possible results for the microgrid. Upon achieving the optimal outcomes, a comparative analysis of the methods was then carried out.

References

ABU, S. M. et al. State of the art of lithium-ion battery material potentials: An analytical evaluations, issues and future research directions. **Journal of Cleaner Production**, [s. l.], v. 394, n. December 2022, p. 136246, 2023. Disponível em: <https://doi.org/10.1016/j.jclepro.2023.136246>

ABUNIMA, H. et al. Two-Stage stochastic optimization for operating a Renewable-Based Microgrid. **Applied Energy**, [s. l.], v. 325, 2022.

ALI DASHTAKI, A. et al. Optimal management algorithm of microgrid connected to the distribution network considering renewable energy system uncertainties. **International Journal of Electrical Power and Energy Systems**, [s. l.], v. 145, 2023.

ANGALAESWARI, S. et al. Efficient Power Management of Grid operated MicroGrid Using Fuzzy Logic Controller (FLC). In: ENERGY PROCEDIA 2017, **Anais**... : Elsevier Ltd, 2017.

AQUILA, G. et al. Wind power generation: An impact analysis of incentive strategies for cleaner energy provision in Brazil. **Journal of Cleaner Production**, [s. l.], v. 137, p. 1100–1108, 2016.

BHATTACHARYA, A.; CHATTERJEE, D.; GOSWAMI, S. K. A fuzzy based improved power sharing methodology for islanded microgrid with hybrid sources. **Electric Power Systems Research**, [s. l.], v. 217, 2023.

BILENDO, F. et al. Applications and Modeling Techniques of Wind Turbine Power Curve for Wind Farms—A Review. **Energies**, [s. l.], v. 16, n. 1, 2023.

CAI, W.; KORDABAD, A. B.; GROS, S. Energy management in residential microgrid using model predictive control-based reinforcement learning and Shapley value. **Engineering Applications of Artificial Intelligence**, [s. l.], v. 119, n. January 2022, p. 105793, 2023. Disponível em: <https://doi.org/10.1016/j.engappai.2022.105793>

CAMACHO, E. F.; BORDONS, C. **Model Predictive Control**. London: Springer, 1999.

CANADIAN SOLAR. **Canadian Solar Brazil**. 2023. Disponível em: <https://www.csisolar.com/br/downloads/>. Acesso em: 26 fev. 2023.

CAO, M. et al. Battery energy storage sizing based on a model predictive control strategy with operational constraints to smooth the wind power. **International Journal of Electrical Power and Energy Systems**, [s. l.], v. 115, 2020.

CARVALHO, D. B.; GUARDIA, E. C.; MARANGON LIMA, J. W. Technical-economic analysis of the insertion of PV power into a wind-solar hybrid system. **Solar Energy**, [s. l.], v. 191, n. February, p. 530–539, 2019. Disponível em: <https://doi.org/10.1016/j.solener.2019.06.070>

CHEN, H. et al. Progress in electrical energy storage system: A critical review. **Progress in Natural Science**, [s. l.], v. 19, n. 3, p. 291–312, 2009. Disponível em: <http://dx.doi.org/10.1016/j.pnsc.2008.07.014>

CHEN, X.; DONG, W.; YANG, Q. Robust optimal capacity planning of grid-connected microgrid considering energy management under multi-dimensional uncertainties. **Applied Energy**, [s. l.], v. 323, 2022.

DANTE, A. W. et al. A Stochastic Approach to Designing Plug-In Electric Vehicle Charging Controller for Residential Applications. **IEEE Access**, [s. l.], v. 10, p. 52876–52889, 2022.

Eletricidade Moderna. 2023. Disponível em:

<https://www.arandanet.com.br/revista/em/guia/ 685-Supercapacitores>. Acesso em: 9 set. 2023.

ENERGY AGENCY, I. **Statistics report Key World Energy Statistics 2021**. [s.l: s.n.]. Disponível em: <https://www.iea.org/reports/key-world-energy-statistics-2021>. Acesso em: 30 abr. 2022.

ERAZO-CAICEDO, D.; MOJICA-NAVA, E.; REVELO-FUELAGÁN, J. Model predictive control for optimal power flow in grid-connected unbalanced microgrids. **Electric Power Systems Research**, [s. l.], v. 209, 2022.

FAHIM, M. et al. Machine Learning-Based Digital Twin for Predictive Modeling in Wind Turbines. **IEEE Access**, [s. l.], v. 10, p. 14184–14194, 2022.

FAN, X. et al. All-temperature batteries enabled by fluorinated electrolytes with non-polar solvents. **Nature Energy**, [s. l.], v. 4, n. 10, p. 882–890, 2019. Disponível em: <http://dx.doi.org/10.1038/s41560-019-0474-3>

FANG, X. et al. Multiple time-scale energy management strategy for a hydrogen-based multi-energy microgrid. **Applied Energy**, [s. l.], v. 328, 2022.

FATHY, A. Bald eagle search optimizer-based energy management strategy for microgrid with renewable sources and electric vehicles. **Applied Energy**, [s. l.], v. 334, n. November 2022, p. 120688, 2023. Disponível em: <https://doi.org/10.1016/j.apenergy.2023.120688>

GALLO, A. B. et al. Energy storage in the energy transition context: A technology review. **Renewable and Sustainable Energy Reviews**, [s. l.], v. 65, p. 800–822, 2016. Disponível em: <http://dx.doi.org/10.1016/j.rser.2016.07.028>

GAUTHAM PRASAD, G. et al. Supercapacitor technology and its applications: A review. **IOP Conference Series: Materials Science and Engineering**, [s. l.], v. 561, n. 1, 2019.

GUERRERO, J. M. et al. Advanced control architectures for intelligent microgridsPart II: Power quality, energy storage, and AC/DC microgrids. **IEEE Transactions on Industrial Electronics**, [s. l.], v. 60, n. 4, p. 1263–1270, 2013.

HAN, Y. et al. Electrical performance and power prediction of a roll-bond photovoltaic thermal array under dewing and frosting conditions. **Energy**, [s. l.], v. 237, p. 121587, 2021. Disponível em: <https://doi.org/10.1016/j.energy.2021.121587>

HARTANI, M. A. et al. Sustainable energy assessment of multi-type energy storage system in direct-current-microgrids adopting Mamdani with Sugeno fuzzy logic-based energy management strategy. **Journal of Energy Storage**, [s. l.], v. 56, 2022.

HE, J. et al. Stochastic Model Predictive Control of Hybrid Energy Storage for Improving AGC Performance of Thermal Generators. **IEEE Transactions on Smart Grid**, [s. l.], v. 13, n. 1, p. 393–405, 2022.

HE, Y. et al. Day-ahead and intraday multi-time scale microgrid scheduling based on light robustness and MPC. **International Journal of Electrical Power and Energy Systems**, [s. l.], v. 144, 2023.

HEIDARY, J.; GHEISARNEJAD, M.; KHOOBAN, M. H. Stability Enhancement and Energy Management of AC-DC Microgrid based on Active Disturbance Rejection Control. **Electric Power Systems Research**, [s. l.], v. 217, n. July 2022, p. 109105, 2023. Disponível em: <https://doi.org/10.1016/j.epsr.2022.109105>

HELSETH, L. E. The nonlinearities in the galvanostatic charging curves of supercapacitors provide insights into charging mechanisms. **Journal of Energy Storage**, [s. l.], v. 55, 2022.

HOW, D. N. T. et al. State-of-Charge Estimation of Li-Ion Battery in Electric Vehicles: A Deep Neural Network Approach. **IEEE Transactions on Industry Applications**, [s. l.], v. 56, n. 5, p. 5565–5574, 2020.

HU, S. et al. Resilient Load Frequency Control of Islanded AC Microgrids Under Concurrent False Data Injection and Denial-of-Service Attacks. **IEEE Transactions on Smart Grid**, [s. l.], v. 14, n. 1, p. 690–700, 2022.

HU, X. et al. Model predictive control of hybrid electric vehicles for fuel economy, emission reductions, and inter-vehicle safety in car-following scenarios. **Energy**, [s. l.], v. 196, 2020.

HUANG, C. et al. Economic and resilient operation of hydrogen-based microgrids: An improved MPC-based optimal scheduling scheme considering security constraints of hydrogen facilities. **Applied Energy**, [s. l.], v. 335, n. February, p. 120762, 2023. Disponível em: <https://doi.org/10.1016/j.apenergy.2023.120762>

JAIN, D.; SAXENA, D. Comprehensive review on control schemes and stability investigation of hybrid AC-DC microgrid. **Electric Power Systems Research**, [s. l.], v. 218, n. November 2022, p. 109182, 2023. Disponível em: <https://doi.org/10.1016/j.epsr.2023.109182>

JIAO, F. et al. Online optimal dispatch based on combined robust and stochastic model predictive control for a microgrid including EV charging station. **Energy**, [s. l.], v. 247, 2022.

JOSÉ, J. R.; F. CAMACHO, E. Centralized and distributed Model Predictive Control for the maximization of the thermal power of solar parabolic-trough plants. **Solar Energy**, [s. l.], v. 204, p. 190–199, 2020.

K/BIDI, F. et al. Multistage power and energy management strategy for hybrid microgrid with photovoltaic production and hydrogen storage. **Applied Energy**, [s. l.], v. 323, 2022.

KHATAMIANFAR, A. et al. Improving wind farm dispatch in the australian electricity market with battery energy storage using model predictive control. **IEEE Transactions on Sustainable Energy**, [s. l.], v. 4, n. 3, p. 745–755, 2013.

KHOKHAR, B.; PARMAR, K. P. S. Utilizing diverse mix of energy storage for LFC performance enhancement of a microgrid: A novel MPC approach. **Applied Energy**, [s. l.], v. 333, n. October 2022, p. 120639, 2023. Disponível em: <https://doi.org/10.1016/j.apenergy.2023.120639>

KIM, W. J. et al. Reserve-Constrained Unit Commitment Considering Adjustable-Speed Pumped-Storage Hydropower and Its Economic Effect in Korean Power System. **Energies**, [s. l.], v. 15, n. 7, 2022.

KUMAR, K.; BAE, S. Dynamic power management based on model predictive control for hybrid-energy-storage-based grid-connected microgrids. **International Journal of Electrical Power and Energy Systems**, [s. l.], v. 143, 2022.

LASSETER, R. H. Smart distribution: Coupled microgrids. In: PROCEEDINGS OF THE IEEE 2011, **Anais**... : Institute of Electrical and Electronics Engineers Inc., 2011.

LEGRY, M. et al. Model Predictive Control-based supervisor for primary support of grid-interactive microgrids. **Control Engineering Practice**, [s. l.], v. 134, n. April 2022, p. 105458, 2023. Disponível em: <https://doi.org/10.1016/j.conengprac.2023.105458>

LEONORI, S. et al. Optimization strategies for Microgrid energy management systems by Genetic Algorithms. **Applied Soft Computing Journal**, [s. l.], v. 86, 2020.

LI, W.; ERICKSON, E. M.; MANTHIRAM, A. High-nickel layered oxide cathodes for lithium-based automotive batteries. **Nature Energy**, [s. l.], v. 5, n. 1, p. 26–34, 2020. Disponível em: <http://dx.doi.org/10.1038/s41560-019-0513-0>

LÓPEZ-BAUTISTA, A. O.; FLORES-TLACUAHUAC, A.; GUTIÉRREZ-LIMÓN, M. A. Robust model predictive control for a nanofluid based solar thermal power plant. **Journal of Process Control**, [s. l.], v. 94, p. 97–109, 2020.

MAGESH, T.; DEVI, G.; LAKSHMANAN, T. Measurement and simulation of power quality issues in grid connected wind farms. **Electric Power Systems Research**, [s. l.], v.

210, n. May, p. 108142, 2022. Disponível em: <https://doi.org/10.1016/j.epsr.2022.108142>

MANSOORHOSEINI, P.; MOZAFARI, B.; MOHAMMADI, S. Islanded AC/DC microgrids supervisory control: A novel stochastic optimization approach. **Electric Power Systems Research**, [s. l.], v. 209, 2022.

MANTHIRAM, A. A reflection on lithium-ion battery cathode chemistry. **Nature Communications**, [s. l.], v. 11, n. 1, p. 1–9, 2020.

MEHTA, S.; BASAK, P. Cascaded dual fuzzy logic controller for stable microgrid operation mitigating effects of natural uncertainty in solar and wind energy sources. **e-Prime - Advances in Electrical Engineering, Electronics and Energy**, [s. l.], v. 5, 2023.

MELLOUK, L. et al. Design and energy management optimization for hybrid renewable energy system- case study: Laayoune region. **Renewable Energy**, [s. l.], v. 139, n. 2019, p. 621–634, 2019. Disponível em: <https://doi.org/10.1016/j.renene.2019.02.066>

MIRJALILI, S.; LEWIS, A. The Whale Optimization Algorithm. **Advances in Engineering Software**, [s. l.], v. 95, p. 51–67, 2016.

NAHATA, P. et al. Hierarchical Control in Islanded DC Microgrids with Flexible Structures. **IEEE Transactions on Control Systems Technology**, [s. l.], v. 29, n. 6, p. 2379–2392, 2021.

NAWAZ, A. et al. Distributed MPC-based energy scheduling for islanded multi-microgrid considering battery degradation and cyclic life deterioration. **Applied Energy**, [s. l.], v. 329, p. 120168, 2023.

OSAKA; OHTA, Y. **2015 54th IEEE Conference on Decision and Control (CDC) date: 15-18 Dec. 2015**. [s.l.] : IEEE, 2015.

OSTERWALD, C. R. **TRANSLATION OF DEVICE PERFORMANCE MEASUREMENTS TO REFERENCE CONDITIONS*Solar Cells**. [s.l: s.n.].

PARHIZI, S. et al. **State of the art in research on microgrids: A review**, Institute of Electrical and Electronics Engineers Inc., 2015.

POLIMENI, S. et al. Development and experimental validation of hierarchical energy management system based on stochastic model predictive control for Off-grid Microgrids. **Advances in Applied Energy**, [s. l.], v. 2, 2021.

RITTER, A. et al. Long-term stochastic model predictive control for the energy management of hybrid electric vehicles using Pontryagin's minimum principle and scenario-based optimization. **Applied Energy**, [s. l.], v. 322, 2022.

RODRÍGUEZ-GÓMEZ, F. et al. Data driven tools to assess the location of photovoltaic facilities in urban areas. **Expert Systems with Applications**, [s. l.], v. 203, n. May, p. 117349, 2022. Disponível em: <https://doi.org/10.1016/j.eswa.2022.117349>

RODRIGUEZ, M.; ARCOS-AVILES, D.; GUINJOAN, F. Simple fuzzy logic-based energy management for power exchange in isolated multi-microgrid systems: A case study in a remote community in the Amazon region of Ecuador. **Applied Energy**, [s. l.], v. 357, 2024.

ROTAS, R. et al. Adaptive Dynamic Building Envelopes with Solar Power Components: Annual Performance Assessment for Two Pilot Sites. **Energies**, [s. l.], v. 16, n. 5, 2023.

SAHRI, Y. et al. Performance improvement of Hybrid System based DFIG-Wind/PV/Batteries connected to DC and AC grid by applying Intelligent Control. **Energy Reports**, [s. l.], v. 9, p. 2027–2043, 2023. Disponível em: <https://doi.org/10.1016/j.egyr.2023.01.021>

SATPATHY, S.; DEBBARMA, S.; BHATTACHARYYA, B. K. An integration of the review of electrode's materials and a new gamma function-based charging methodology of supercapacitor for high current applications. In: MATERIALS TODAY: PROCEEDINGS 2019, **Anais**... : Elsevier Ltd, 2019.

SHABANI, M. et al. The impact of battery operating management strategies on life

cycle cost assessment in real power market for a grid-connected residential battery application. **Energy**, [s. l.], v. 270, n. January, p. 126829, 2023. Disponível em: <https://doi.org/10.1016/j.energy.2023.126829>

SHAN, Y.; HU, J.; LIU, H. A Holistic Power Management Strategy of Microgrids Based on Model Predictive Control and Particle Swarm Optimization. **IEEE Transactions on Industrial Informatics**, [s. l.], v. 18, n. 8, p. 5115–5126, 2022.

SHETGAONKAR, A. et al. Model predictive control and protection of MMC-based MTDC power systems. **International Journal of Electrical Power and Energy Systems**, [s. l.], v. 146, 2023.

SKELETON+. **Skeleton Supercapacitor System**. [s.d.]. Disponível em: <https://www.skeletontech.com/en/systems?hsLang=en>. Acesso em: 19 jan. 2023.

SPYKER, R. L. Classical equivalent circuit parameters for a double-layer capacitor. **IEEE Transactions on Aerospace and Electronic Systems**, [s. l.], v. 36, n. 3 PART 1, p. 829–836, 2000.

STEPANOV, A. Outlook supercapacitors uninterruptible supplies Galkin',. [s. l.], p. 2–5, 2006.

SUN, T. et al. Estimating the spatial distribution of solar photovoltaic power generation potential on different types of rural rooftops using a deep learning network applied to satellite images. **Applied Energy**, [s. l.], v. 315, n. March, p. 119025, 2022. Disponível em: <https://doi.org/10.1016/j.apenergy.2022.119025>

TORKAN, R.; ILINCA, A.; GHORBANZADEH, M. A genetic algorithm optimization approach for smart energy management of microgrid. **Renewable Energy**, [s. l.], v. 197, p. 852–863, 2022.

TOSTADO-VÉLIZ, M. et al. A Stochastic-IGDT model for energy management in isolated microgrids considering failures and demand response. **Applied Energy**, [s. l.], v. 317, 2022.

VIEIRA, P. A. V; BORTONI, E. C.; BRETAS, A. S. A New Approach of Conti-Varlet Method Applied to a PV System to Size a Battery Energy Storage; A New Approach of Conti-Varlet Method Applied to a PV System to Size a Battery Energy Storage. In: 2019 IEEE MILAN POWERTECH 2019, **Anais**... [s.l: s.n.]

WANG, B.; CAI, G.; YANG, D. Dispatching of a Wind Farm Incorporated with Dual-Battery Energy Storage System Using Model Predictive Control. **IEEE Access**, [s. l.], v. 8, p. 144442–144452, 2020.

Wind Turbine Models. 2022. Disponível em: <https://en.wind-turbine-models.com/turbines/1686-hummer-h17.0-50kw>. Acesso em: 31 ago. 2023.

WU, L. et al. Economic model predictive control of integrated energy systems: A multi-time-scale framework. **Applied Energy**, [s. l.], v. 328, 2022.

ZHAO, J.; WANG, W.; GUO, C. Hierarchical optimal configuration of multi-energy microgrids system considering energy management in electricity market environment. **International Journal of Electrical Power and Energy Systems**, [s. l.], v. 144, 2023.

ZHAO, Z. et al. Distributed Robust Model Predictive Control-Based Energy Management Strategy for Islanded Multi-Microgrids Considering Uncertainty. **IEEE Transactions on Smart Grid**, [s. l.], v. 13, n. 3, p. 2107–2120, 2022.

ZHONG, X. et al. Optimal energy management for multi-energy multi-microgrid networks considering carbon emission limitations. **Energy**, [s. l.], v. 246, 2022.

ZHU, J. hong et al. Economic dispatching of Wind/ photovoltaic/ storage considering load supply reliability and maximize capacity utilization. **International Journal of Electrical Power and Energy Systems**, [s. l.], v. 147, n. November 2022, p. 108874, 2023. Disponível em: <https://doi.org/10.1016/j.ijepes.2022.108874>

Appendix A

The Hummer H17.0-50kW turbine datasheet	
Power	
Rated power:	50 kW
Cut-in wind speed:	3.5 m/s
Rated wind speed:	9.5 m/s
Cut-out wind speed:	20.0 m/s
Survival wind speed:	50.0 m/s
Rotor	
Diameter	17 m
Swept area	227 m²
Number of blades	3
Rotor speed, max	85.0 U/min
Tipspeed	76 m/s
Type	8m
Material	Fiberglass reinforced composite.RTM
Power density 1	220.3 W/m²
Power density 2	4.5 m²/kW

BiHiKu

HIGH POWER BIFACIAL POLY PERC MODULE

400 W ~ 425 W

UP TO 30% MORE POWER FROM THE BACK SIDE
CS3W-400|405|410|415|420|425PB-AG

MORE POWER

EXTRA POWER — Up to 30% more power from the back side

24 % higher front side power than conventional modules

41°C — Low NMOT: 41 ± 3 °C
Low temperature coefficient (Pmax): -0.36 % / °C

FRONT   BACK

12 Years — Enhanced Product Warranty on Materials and Workmanship*

30 Years — Linear Power Performance Warranty*

1st year power degradation no more than 2%

ELECTRICAL DATA | STC*

		Nominal Max. Power (Pmax)	Opt. Operating Voltage (Vmp)	Opt. Operating Current (Imp)	Open Circuit Voltage (Voc)	Short Circuit Current (Isc)	Module Efficiency
CS3W-400PB-AG		400 W	38.7 V	10.34 A	47.2 V	10.90 A	17.9%
	5%	420 W	38.7 V	10.86 A	47.2 V	11.45 A	18.8%
Bifacial Gain**	10%	440 W	38.7 V	11.37 A	47.2 V	11.99 A	19.7%
	20%	480 W	38.7 V	12.41 A	47.2 V	13.08 A	21.5%
	30%	520 W	38.7 V	13.44 A	47.2 V	14.17 A	23.3%
CS3W-405PB-AG		405 W	38.9 V	10.42 A	47.4 V	10.98 A	18.1%
	5%	425 W	38.9 V	10.94 A	47.4 V	11.53 A	19.0%
Bifacial Gain**	10%	446 W	38.9 V	11.46 A	47.4 V	12.08 A	20.0%
	20%	486 W	38.9 V	12.50 A	47.4 V	13.18 A	21.8%
	30%	527 W	38.9 V	13.55 A	47.4 V	14.27 A	23.6%
CS3W-410PB-AG		410 W	39.1 V	10.49 A	47.6 V	11.06 A	18.4%
	5%	431 W	39.1 V	11.01 A	47.6 V	11.61 A	19.3%
Bifacial Gain**	10%	451 W	39.1 V	11.54 A	47.6 V	12.17 A	20.2%
	20%	492 W	39.1 V	12.59 A	47.6 V	13.27 A	22.0%
	30%	533 W	39.1 V	13.64 A	47.6 V	14.38 A	23.9%
CS3W-415PB-AG		415 W	39.3 V	10.56 A	47.8 V	11.14 A	18.6%
	5%	436 W	39.3 V	11.09 A	47.8 V	11.70 A	19.5%
Bifacial Gain**	10%	457 W	39.3 V	11.62 A	47.8 V	12.25 A	20.4%
	20%	498 W	39.3 V	12.67 A	47.8 V	13.37 A	22.3%
	30%	540 W	39.3 V	13.73 A	47.8 V	14.48 A	24.2%
CS3W-420PB-AG		420 W	39.5 V	10.64 A	48.0 V	11.26 A	18.8%
	5%	441 W	39.5 V	11.17 A	48.0 V	11.82 A	19.7%
Bifacial Gain**	10%	462 W	39.5 V	11.70 A	48.0 V	12.39 A	20.7%
	20%	504 W	39.5 V	12.77 A	48.0 V	13.51 A	22.6%
	30%	546 W	39.5 V	13.83 A	48.0 V	14.64 A	24.4%
CS3W-425PB-AG		425 W	39.7 V	10.71 A	48.2 V	11.29 A	19.0%
	5%	446 W	39.7 V	11.25 A	48.2 V	11.85 A	20.0%
Bifacial Gain**	10%	468 W	39.7 V	11.79 A	48.2 V	12.42 A	20.9%
	20%	510 W	39.7 V	12.85 A	48.2 V	13.55 A	22.8%
	30%	553 W	39.7 V	13.93 A	48.2 V	14.68 A	24.8%

* Under Standard Test Conditions (STC) of irradiance of 1000 W/m², spectrum AM 1.5 and cell temperature of 25°C.

ELECTRICAL DATA | NMOT*

	Nominal Max. Power (Pmax)	Opt. Operating Voltage (Vmp)	Opt. Operating Current (Imp)	Open Circuit Voltage (Voc)	Short Circuit Current (Isc)
CS3W-400PB-AG	299 W	36.2 V	8.27 A	44.5 V	8.79 A
CS3W-405PB-AG	303 W	36.3 V	8.33 A	44.7 V	8.85 A
CS3W-410PB-AG	307 W	36.5 V	8.39 A	44.8 V	8.92 A
CS3W-415PB-AG	310 W	36.7 V	8.45 A	45.0 V	8.98 A
CS3W-420PB-AG	314 W	36.9 V	8.51 A	45.2 V	9.08 A
CS3W-425PB-AG	318 W	37.1 V	8.57 A	45.4 V	9.10 A

* Under Nominal Module Operating Temperature (NMOT), irradiance of 800 W/m², spectrum AM 1.5, ambient temperature 20°C, wind speed 1 m/s.

MECHANICAL DATA

Specification	Data
Cell Type	Poly-crystalline
Cell Arrangement	144 [2 X (12 X 6)]
Dimensions	2132 × 1048 × 30 mm (83.9 × 41.3 × 1.2 in)
Weight	28.4 kg (62.6 lbs)
Front / Back Glass	2.0 mm heat strengthened glass with anti-reflective coating
Frame	Anodized aluminium alloy
J-Box	IP68, 3 bypass diodes
Cable	4.0 mm² (IEC), 12 AWG (UL)
Cable Length (Including Connector)	400 mm (15.7 in) (+) / 280 mm (11.0 in) (-) or customized length*
Connector	T6 or T4 series or MC4-EVO2
Per Pallet	33 pieces
Per Container (40' HQ)	660 pieces or 627 pieces (only for US)

* For detailed information, please contact your local Canadian Solar sales and technical representatives.

Appendix B

Section I)

The modeling of the battery is shown below.

Applying Kirchhoff's Voltage Law to the circuit in FIGURE 4 yields:

$$E - V_{Cbat} - R_{s(bat)} i_{bat} - V_{bat} = 0 \qquad \text{B-0-1}$$

$$V_{Cbat} = R_{p(bat)}(i_{bat} - i_{Cbat}) \qquad \text{B-0-2}$$

By taking the time derivative of both sides of $V_{Cbat} = R_{p(bat)}(i_{bat} - i_{Cbat})$ B-0-2 and multi-

$$\underbrace{C_{bat}\frac{dV_{Cbat}}{dt}}_{i_{Cbat}} = C_{bat}R_{p(bat)}\frac{di_{bat}}{dt} - C_{bat}R_{p(bat)}\frac{di_{Cbat}}{dt}$$

plying all terms by C_{bat}, B-0-3 can be derived.

Next, the left side of the equation is isolated to obtain $\dfrac{di_{Cbat}}{dt} = \dfrac{di_{bat}}{dt} - \dfrac{i_{Cbat}}{R_{p(bat)}C_{bat}}$ B-0-4,

which represents the time derivative of i_{Cbat}.

$$\underbrace{C_{bat}\frac{dV_{Cbat}}{dt}}_{i_{Cbat}} = C_{bat}R_{p(bat)}\frac{di_{bat}}{dt} - C_{bat}R_{p(bat)}\frac{di_{Cbat}}{dt} \qquad \text{B-0-3}$$

$$\frac{di_{Cbat}}{dt} = \frac{di_{bat}}{dt} - \frac{i_{Cbat}}{R_{p(bat)}C_{bat}} \qquad \text{B-0-4}$$

From $E - V_{Cbat} - R_{s(bat)} i_{bat} - V_{bat} = 0$ B-0-1 and $V_{Cbat} = R_{p(bat)}(i_{bat} - i_{Cbat})$ B-0-2:

$$V_{bat} = E - R_{p(bat)}(i_{bat} - i_{Cbat}) - R_{s(bat)}i_{bat} \qquad \text{B-0-5}$$

$$V_{bat} = E + R_{p(bat)}i_{Cbat} - (R_{p(bat)} + R_{s(bat)})i_{bat} \qquad \text{B-0-6}$$

The process of computing UC power is analogous to that of battery power, wherein the UC circuit model is subject to analysis using Kirchhoff's Voltage Law.

$$V_{\text{UC}} = R_{\text{p(UC)}}(i_{\text{UC}} - i_{\text{load}})$$ B-7

$$C_{UC}\frac{dV_{UC}}{dt} = R_{p(UC)}C_{UC}\frac{di_{UC}}{dt} - R_{p(UC)}C_{UC}\frac{di_{load}}{dt}$$ B-8

$$\frac{di_{load}}{dt} = \frac{di_{UC}}{dt} - \frac{i_{UC}}{R_{pUC}C_{UC}}$$ B-9

Furthermore,

$$V_{\text{UC}} - R_{\text{s(UC)}}i_{\text{load}} - V_{\text{load}} = 0$$ B-10

Replacing $V_{\text{UC}} = R_{\text{p(UC)}}(i_{\text{UC}} - i_{\text{load}})$ B-7 in $C_{UC}\frac{dV_{UC}}{dt} = R_{p(UC)}C_{UC}\frac{di_{UC}}{dt} - R_{p(UC)}C_{UC}\frac{di_{load}}{dt}$

B-8, it is found:

$$V_{\text{load}} = R_{\text{p(UC)}}i_{\text{UC}} - (R_{\text{p(UC)}} + R_{\text{s(UC)}})i_{\text{load}}$$ B-0-7

Therefore, the determination of power that the ultra-capacitor delivers is conducted in accordance with B-12 $P_{\text{UC}} = R_{\text{p(UC)}}i^2{}_{\text{UC}} - R_{\text{p(UC)}}i_{\text{load}}i_{\text{UC}}$ 3-2.

$$P_{\text{UC}} = i_{\text{UC}}V_{\text{UC}}$$ B-12

Section II) MPC modeling

MPC output predictions can be derived from eq. $\begin{aligned}x(k+1) &= Ax(k) + Bu(k)\\ y(k) &= Cx(k) + Dr(k)\end{aligned}$ 4-1. The

following modeling is based on the works of Khatamianfar et al. (2013) and Wang; Cai; Yang (2020a).

$$\begin{aligned}
y(k+1) &= Cx(k+1) + Dr(k+1)\\
&= C\underbrace{\left[Ax(k) + Bu(k)\right]}_{=x(k+1)\ from\ eq.4-1} + Dr(r+1)\\
&= CAx(k) + CBu(k) + Dr(k+1)
\end{aligned}$$

$$\begin{aligned}
y(k+2) &= Cx(k+2) + Dr(r+2)\\
&= C\left[Ax(k+1) + Bu(k+1)\right] + Dr(k+2)\\
&= C\left[A\left[Ax(k) + Bu(k)\right] + Bu(k+1)\right] + Dr(k+2)\\
&= CA^2 x(k) + CABu(k) + CBu(k+1) + Dr(k+2)
\end{aligned}$$
$$\vdots$$
$$y(k+m_c) = CA^{m_c} x(k) + CA^{(m_c-1)}Bu(k) + \cdots + CBu(k+m_c-1) + Dr(k+m_c)$$

The parameters in eqs. $y = G_y x(k) + \theta_y u + Kr$ 4-4 and $\mathbf{x} = G_x x(k) + \theta_x u$ 4-5 are assigned as:

$$G_y = \begin{bmatrix} CA \\ CA^2 \\ \vdots \\ CA^{m_c} \end{bmatrix}_{qm_c \times n} \quad \theta_y = \begin{bmatrix} CB & 0 & 0 & \cdots & 0 \\ CAB & CB & 0 & \cdots & 0 \\ CA^2B & CAB & CB & \cdots & 0 \\ \vdots & \vdots & \vdots & \ddots & \vdots \\ CA^{m_c-1}B & CA^{m_c-2}B & CA^{m_c-3}B & \cdots & CB \end{bmatrix}_{qm_c \times pm_c} \quad K = \begin{bmatrix} D & 0 & \cdots & 0 \\ 0 & D & \cdots & 0 \\ \vdots & \vdots & \ddots & \vdots \\ 0 & 0 & \cdots & D \end{bmatrix}_{qm_c \times m_c}$$

$$y = \begin{bmatrix} y(k+1) \\ y(k+2) \\ \vdots \\ y(k+m_c) \end{bmatrix}_{m_c \times 1} \quad u = \begin{bmatrix} u(k) \\ u(k+1) \\ \vdots \\ u(k+m_c-1) \end{bmatrix}_{pm_c \times 1} \quad r = \begin{bmatrix} r(k) \\ r(k+1) \\ \vdots \\ r(k+m_c-1) \end{bmatrix}_{m_c \times 1}$$

$$x = \begin{bmatrix} x(k+1) \\ x(k+2) \\ \vdots \\ x(k+m_c) \end{bmatrix}_{nm_c \times 1} \quad G_x = \begin{bmatrix} A \\ A^2 \\ \vdots \\ A^{m_c} \end{bmatrix}_{nm_c \times n} \quad \theta_x = \begin{bmatrix} B & 0 & 0 & \cdots & 0 \\ AB & AB & 0 & \cdots & 0 \\ A^2B & AB & B & \cdots & 0 \\ \vdots & \vdots & \vdots & \ddots & \vdots \\ A^{m_c-1}B & A^{m_c-1}B & A^{m_c-1}B & \cdots & B \end{bmatrix}_{nm_c \times pm_c}$$

The parameters in eq. $J = \left(y - y_{ref} \right)^T W_y \left(y - y_{ref} \right) + u^T W_u u$ 4-6 are defined as:

$$y_{ref} = \begin{bmatrix} y_{ref}(k+1) \\ y_{ref}(k+2) \\ \vdots \\ y_{ref}(k+m_c) \end{bmatrix}_{m_c \times 1} \quad W_y = \begin{bmatrix} w_y & 0 & \cdots & 0 \\ 0 & w_y & \cdots & 0 \\ \vdots & \vdots & \ddots & \vdots \\ 0 & 0 & \cdots & w_y \end{bmatrix}_{qm_c \times qm_c} \quad W_u = \begin{bmatrix} w_u & 0 & \cdots & 0 \\ 0 & w_u & \cdots & 0 \\ \vdots & \vdots & \ddots & \vdots \\ 0 & 0 & \cdots & w_u \end{bmatrix}_{pm_c \times pm_c}$$

The parameter U_{max} in eq. $IU \le U_{\max} \quad and \quad -IU \le -U_{\max}$ 4-7 is designed as:

$$U_{\max} = \begin{bmatrix} u_{\max(bat)} \\ u_{\max(UC)} \\ \vdots \\ u_{\max(bat)} \\ u_{\max(UC)} \end{bmatrix}_{pm_c \times 1}$$

Vectors and matrices used in eq. $Q\theta_x U \le -QG_x x(k) + Q_r \left(SOC - SOC_{\min} \right) \quad and \quad -Q\theta_x U \le QG_x x(k) + Q_r \left(SOC_{\max} - SOC \right)$ 4-10:

$$SOC - \frac{QX}{Q_r} \ge SOC_{\min} \quad and \quad SOC - \frac{QX}{Q_r} \le SOC_{\max} \qquad 4-9$$

$$Q = \Delta t \begin{bmatrix} 1 & 0 & 0 & 0 & \cdots & 0 & 0 & 0 & 0 \\ 0 & 0 & 0 & 1 & \cdots & 0 & 0 & 0 & 0 \\ \vdots & \vdots & \vdots & \vdots & \ddots & \vdots & \vdots & \vdots & \vdots \\ 0 & 0 & 0 & 0 & \cdots & 1 & 0 & 0 & 0 \\ 0 & 0 & 0 & 0 & \cdots & 0 & 0 & 0 & 1 \end{bmatrix}_{pm_c \times nm_c} \qquad Q_r = \begin{bmatrix} q_{r(bat)} & 0 & 0 & \cdots & 0 \\ 0 & q_{r(UC)} & 0 & \cdots & 0 \\ \vdots & \vdots & \ddots & \vdots & \vdots \\ 0 & 0 & \cdots & q_{r(bat)} & 0 \\ 0 & 0 & \cdots & 0 & q_{r(UC)} \end{bmatrix}_{pm_c \times pm_c}$$

$$SOC_{min} = \begin{bmatrix} soc_{min(bat)} \\ soc_{min(UC)} \\ \vdots \\ soc_{min(bat)} \\ soc_{min(UC)} \end{bmatrix}_{pm_c \times 1} \qquad SOC_{max} = \begin{bmatrix} soc_{max(bat)} \\ soc_{max(UC)} \\ \vdots \\ soc_{max(bat)} \\ soc_{max(UC)} \end{bmatrix}_{pm_c \times 1}$$

The parameters used in $\Omega U \le \omega$ 4-12.

$$U_{opt} = \begin{bmatrix} u_{opt}(k) \\ u_{opt}(k+1) \\ \vdots \\ u_{opt}(k+m_c-1) \end{bmatrix}_{m_c \times 1} \qquad \Omega = \begin{bmatrix} I \\ -I \\ Q\theta_x \\ -Q\theta_x \end{bmatrix} \qquad \omega = \begin{bmatrix} U_{max} \\ U_{max} \\ -QG_x x(k) + Q_r \left(SOC - SOC_{min} \right) \\ QG_x x(k) + Q_r \left(SOC - SOC_{min} \right) \end{bmatrix}$$